

Summer 2021

Quality Assurance of Lightweight Structures via Phase-based Motion Estimation

Ikenna E. Ifekaonwu

Follow this and additional works at: <https://digitalcommons.georgiasouthern.edu/etd>



Part of the [Dynamics and Dynamical Systems Commons](#), [Electrical and Electronics Commons](#), [Mechanical Engineering Commons](#), [Operations Research, Systems Engineering and Industrial Engineering Commons](#), [Polymer and Organic Materials Commons](#), and the [Signal Processing Commons](#)

Recommended Citation

Ifekaonwu, Ikenna E., "Quality Assurance of Lightweight Structures via Phase-based Motion Estimation" (2021). *Electronic Theses and Dissertations*. 2309.
<https://digitalcommons.georgiasouthern.edu/etd/2309>

This thesis (open access) is brought to you for free and open access by the Graduate Studies, Jack N. Averitt College of at Digital Commons@Georgia Southern. It has been accepted for inclusion in Electronic Theses and Dissertations by an authorized administrator of Digital Commons@Georgia Southern. For more information, please contact digitalcommons@georgiasouthern.edu.

QUALITY ASSURANCE OF LIGHTWEIGHT STRUCTURES VIA PHASE-BASED MOTION ESTIMATION

by

IKENNA IFEKAONWU

(Under the Direction of Jinki Kim)

ABSTRACT

In recent years, lightweight structures have become mature and adopted in various applications. The importance of quality assurance cannot be overemphasized hence extensive research has been conducted to assess the quality of lightweight structures. This study investigates a novel process that exploits motion magnification to investigate the damage characteristics of lightweight mission-critical parts. The goal is to assure the structural integrity of 3D printed structures and composite structures by determining the inherent defects present in the part by exploiting their vibration characteristics. The minuscule vibration of the structure was recorded with the aid of a high-speed digital camera, and the motion was estimated by applying a phase-based algorithm. The spectral information was compared with the results obtained by a laser displacement sensor for validation. Then, the video-based results were used to perform damage identification by comparing the extracted information with that of a baseline. The resonance frequencies and the corresponding operational mode shapes of the test structure were obtained using the motion magnification algorithm by applying a bandpass filter around selected resonant frequencies. The resonance frequency and operational mode shape are quantified to compare the damaged structure with the baseline. The damage characteristics depending on the location and depth of damages were experimentally explored and numerically analyzed. Overall, this study provides an accurate, easily available, and fast approach to structural health monitoring, utilizing video-based vibration analysis. It is envisioned that this study will provide a foundation for both commercial and non-commercial purposes exploiting the straightforward and low-cost implementation of the video-based methods.

INDEX WORDS: Motion magnification, Additive manufacturing, Composite material, Modal analysis, Structural health monitoring

QUALITY ASSURANCE OF LIGHTWEIGHT STRUCTURES VIA PHASE-BASED
MOTION ESTIMATION

by

IKENNA EZEKIEL IFEKAONWU

B. Eng., Federal University of Technology, Nigeria, 2014

A Thesis Submitted to the Graduate Faculty of Georgia Southern University in Partial

Fulfillment of the Requirements for the Degree

MASTER OF SCIENCE

© 2021

IKENNA IFEKAONWU

All Rights Reserved

QUALITY ASSURANCE OF LIGHTWEIGHT STRUCTURES VIA PHASE-BASED
MOTION ESTIMATION

by

IKENNA IFEKAONWU

Major Professor: Jinki Kim

Committee: Ermias Koricho

JungHun Choi

Electronic Version Approved:
July 2021

DEDICATION

This achievement would not have been possible without the tremendous support of my uncle Achebe Ekpo, who not only contributed financially to the completion of my master's program but was also available to offer moral and academic support from the beginning of my bachelors' program till this day. I want to appreciate my brother Kenneth Ifekaonwu for his support and always being there to motivate and inspire me towards excellence. I also want to appreciate Olukotun Oludamilare and Emeka Onyejizu for the key role they played in my quest to pursue a master's degree program at Georgia Southern University and for their academic and professional advice. My immense gratitude to my parents Innocent and Ijeoma Ifekaonwu for their belief that education is the right way for a better society.

ACKNOWLEDGMENTS

I would like to appreciate my supervisor and advisor Dr. Jinki Kim for his mentorship and encouragement towards the completion of this thesis. His words and guidance made a tremendous impact in my growth as a researcher and an engineer. Thanks to my thesis committee, Dr. Ermias Koricho and Dr. JungHun Choi, for insights and dedication to the review of my write-ups at different stages of this work. I would also like to thank my research colleague Kenneth Nwagu and Micah Kimutai for their contributions and assistance towards the completion of this work. My gratitude goes to the department chair Dr. Brian Vlcek for his guidance towards the completion of my master's program.

TABLE OF CONTENTS

	Page
ACKNOWLEDGMENTS	3
LIST OF TABLES	6
LIST OF FIGURES	7
CHAPTER 1	10
INTRODUCTION	10
Structural Health Monitoring	10
Additive Manufacturing	12
Composite Structures	13
Camera Based Measurement	14
Thesis Structure	15
CHAPTER 2	17
LITERATURE REVIEW	17
CHAPTER 3	24
PROBLEM STATEMENT AND RESEARCH OBJECTIVE	24
Problem Statement	24
Research Objective and New Idea	24
CHAPTER 4	26
METHODOLOGY	26
Experimental Overview	26
Equipment and Experimental Setup	26
Material Selection	28
Additive Manufacturing of PLA	30
Model Design and Fabrication	30
Testing using Laser Displacement Sensor	31
Phase Based Approach	32
Phase-Based Motion Magnification Process	36
Numerical Analysis	38
Modal Assurance Criterion (MAC)	39

CHAPTER 5	41
RESULTS AND ANALYSIS	41
Resonant Frequency Measurements	41
Validation of the Phase-based Measurements	44
Damage Identifications	47
Measurement of Severity of Defect	48
Measurement of Varying Void Location	51
Motion Magnification	53
Comparison of Experimental Result with the Simulation	58
Modal Assurance Criterion (MAC)	59
Glass Fiber Reinforced Plastic (GFRP) Results	67
Numerical Result of GFRP	72
CHAPTER 6	78
CONCLUSION AND FUTURE WORKS	78
Conclusion	78
Future Works	79
REFERENCES	80

LIST OF TABLES

	Page
Table 1: Material Dimension of PLA	28
Table 2: Mass of the PLA Samples.....	42
Table 3: Frequencies Extracted using Phase-based Approach	43
Table 4: Frequency Comparison between LDS and Phase-based Approach.....	44
Table 5: Frequency Comparison of a Healthy Baseline with Different Severity of Defect	49
Table 6: Frequency Comparison of a Healthy Baseline with Defect at Different Locations	52
Table 7: Motion Magnification Input Parameters.....	54
Table 8: Frequency Comparison of Healthy Baseline with Experimental Result	58
Table 9: Dimension and Mass of GFRP	68
Table 10: Frequency of Baseline and Defective Composite Material	69
Table 11: Material Properties of GFRP used for Numerical Analysis	73
Table 12: Frequency Comparison of Phase based with Numerical Analysis of GFRP Baseline .	73

LIST OF FIGURES

	Page
Figure 1: U.S. SHM Market Projections from year 2015 - 2025 (Coherent Market Insight 2020)	11
Figure 2: Global SHM Market Analysis for 2017 (Coherent Market Insight 2020)	11
Figure 3: Defects in 3D Printing. (Molitch-Hou 2017)	17
Figure 4: 3D-DIC System Demonstration (Dantec Dynamics n.d)	19
Figure 5: X-Ray Microtomography Showing Pores at Different Scan Speed (Koslow 2016).....	20
Figure 6: Schematic Diagram of the Video Magnification process.....	27
Figure 7: Experimental Setup	27
Figure 8: Schematics of the Experimental Sample Dimension	29
Figure 9: Experimental Setup showing the Dimension of the Sample	29
Figure 10: 3D Model of a PLA Beam.....	31
Figure 11: Schematic Layout of a Laser Displacement Sensor	32
Figure 12: Schematic Layout of the Phase Based Motion Estimation Process	33
Figure 13: Complex Gabor Wavelets with 4 Orientations Different Orientation for both Real and Imaginary	34
Figure 14: Schematic Representation of Phase-Based Motion Magnification	37
Figure 15: 3D PLA Model Showing the Fixed Support and Applied Force at the Edge	38
Figure 16: 3D PLA Model Mesh Selection	39
Figure 17: Original Image from the Video	41
Figure 18: Mask Showing Pixels from the Image	41
Figure 19: Mask showing Pixels with extracted displacement using the mean threshold.....	43
Figure 20: Resonant Frequencies of PLA Samples	44
Figure 21: Resonant Frequencies Comparison of LDS with Phase-based Motion Estimation	45
Figure 22: Frequency Response of Baseline PLA using LDS in Comparison with the Phase-based	46
Figure 23: Resonant Frequencies of Baseline of PLA using ANSYS, LDS and Phase-based Motion Estimation	47
Figure 24: 3D Printed Test Model of a PLA Depicting the Defect in the Beam	48

Figure 25: Frequency Response Representation of Phase-based Motion Estimation of Healthy and Varying Degree of Defect of PLA	50
Figure 26: Graphical Representation of Different Frequency Modes of PME for Healthy and Different Degree of Defect	51
Figure 27: Graphical Representation of Different Frequency Modes of Healthy and Defective beam at Different Location using Phase-based Motion Estimation.....	52
Figure 28: Original Image of the PLA.....	54
Figure 29: Second Mode Shape magnification of the PLA	54
Figure 30: Frame before Magnification.....	55
Figure 31: First Mode Shape.....	55
Figure 32: Second Mode Shape	55
Figure 33: Third mode shape	56
Figure 34: Graphical Representation of Operational Mode shapes of Phase-based method for Healthy Beam.....	56
Figure 35: Theoretical Mode Shapes	57
Figure 36: Numerical Simulation of the Operational mode shape of the PLA Compared with the Experimental Results	59
Figure 37: The MAC Estimation of the mode shapes using Phase-based Motion Magnification	60
Figure 38: Frame at Maximum Displacement of the Defective PLA for the First Mode frequency of 36.16Hz and Magnification Factor of 20.....	61
Figure 39: Frame at Maximum Displacement of the Defective PLA for the Second Mode frequency of 229.04Hz and Magnification Factor of 100.....	61
Figure 40: Frame at Maximum Displacement of the Defective PLA for the Second Mode frequency of 229.04Hz and Magnification Factor of 200.....	62
Figure 41: First Operational Mode Shape of Damaged PLA Compared with Healthy Baseline at its Maximum Deflection	63
Figure 42: Second Mode Shape of Damaged PLA Compared with Healthy Baseline at its Maximum Deflection	63
Figure 43: Fourth Mode Shape of Damaged PLA Compared with Healthy Baseline at its Maximum Deflection	64
Figure 44: Estimated MAC Value of Operating Mode Shapes for Baseline and Damaged PLA	64
Figure 45: First Mode Shape of Damaged PLA at Different Location Compared with Healthy Baseline at its Maximum Deflection.....	65

Figure 46: Second Mode Shape of Damaged PLA at Different Location Compared with Healthy Baseline at its Maximum Deflection.....	66
Figure 47: Fourth Mode Shape of Damaged PLA at Different Location Compared with Healthy Baseline at its Maximum Deflection.....	66
Figure 48: Estimated MAC Value of Operating Mode Shapes for Baseline and Damaged PLA at Different Location.....	67
Figure 49: Image of the GFRP Baseline Material	68
Figure 50: Image of the Defective GFRP Material.....	68
Figure 51: Frequency Response of Baseline GFRP.....	69
Figure 52: Frequency Response Comparison of Healthy and Defective GFRP using Phase-based motion Estimation.....	70
Figure 53: Original Video Frame of GFRP without Magnification	71
Figure 54: Image Frame at Maximum Displacement of the Magnified GFRP for the First Mode for Frequency of 60.30Hz, and Magnification Factor of 20	71
Figure 55: Image Frame at Maximum Displacement of the Magnified GFRP for the Second Mode Frequency of 376.42Hz, and Magnification Factor of 200	72
Figure 56: Frequency Comparison of Phase-based method and Numerical Analysis of GFRP ..	73
Figure 57: First Mode Frequency of GFRP	74
Figure 58: Second Mode Frequency of GFRP.....	74
Figure 59: Third Mode Frequency of GFRP.....	75
Figure 60: Fifth Mode Frequency of GFRP.....	75
Figure 61: First Mode Shape of Defective GFRP Compared with Healthy Baseline at its Maximum Deflection	76
Figure 62: Second Mode Shape of Defective GFRP Compared with Healthy Baseline at its Maximum Deflection	76
Figure 63: Estimated MAC Value of the Operational Mode Shapes of the Baseline and Damaged PLA.....	77

CHAPTER 1

INTRODUCTION

Structural Health Monitoring

Monitoring and proper maintenance of structures are vital requirements of today's society. Structural Health Monitoring (SHM) essentially examines the state of the present condition of structural systems to assess their functional fitness and performance levels. If the condition assessment envisaged indicates a deviation from that of a desired one, then that structure may need corrective maintenance or a complete replacement. SHM is an essential component in reliability engineering, since it helps engineers determine a potential risk involved. When successfully employed, SHM enables the reduction of long- or short-term costs, and particularly saves lives and properties. Large, complex, and costly engineering structures are constructed to last for a longer life span.

The scope of SHM includes structural assessment, monitoring and control. Structural monitoring has become a necessity and it is no longer optional as legal mandates have been imposed on safety and security of public properties, health monitoring is also supported and funded by government agencies. For example, the South Carolina Department of Transportation used a sensor-based monitoring method for its structural monitoring of bridges which resulted in savings of about USD 5 million in 2014, this increased savings in SHM is expected to create demand for SHM globally. The global SHM market size was valued at about USD 1.22 billion in 2017, it was projected to reach USD 1.89 billion by 2020, at a compound annual growth rate of 13.9%, between 2019 and 2027 (Coherent Market Insight 2020).

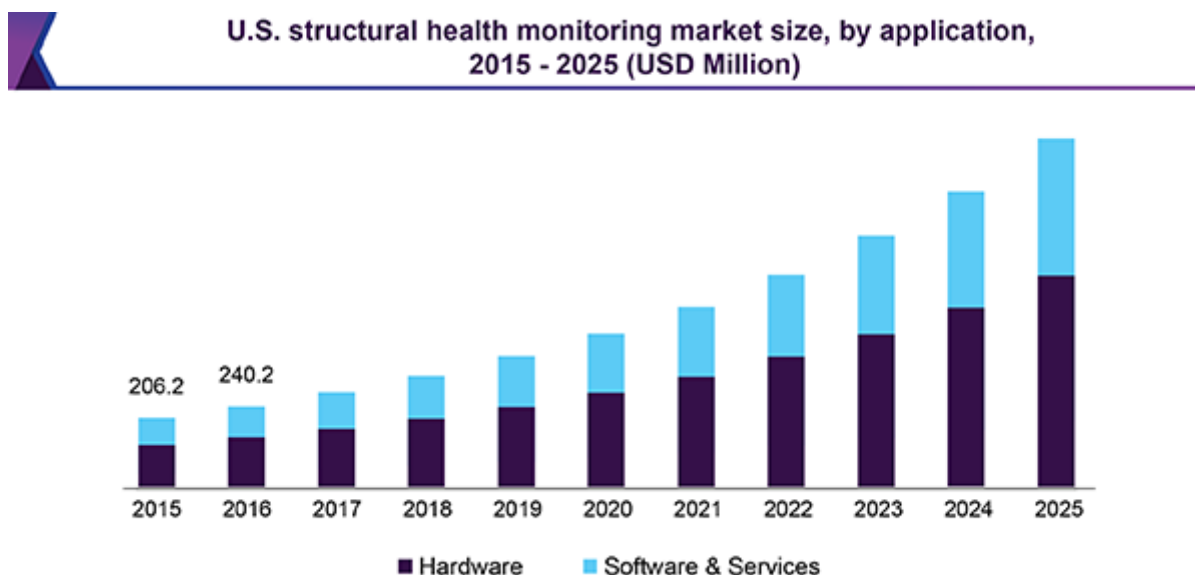


Figure 1: U.S. SHM Market Projections from year 2015 - 2025 (Coherent Market Insight 2020)

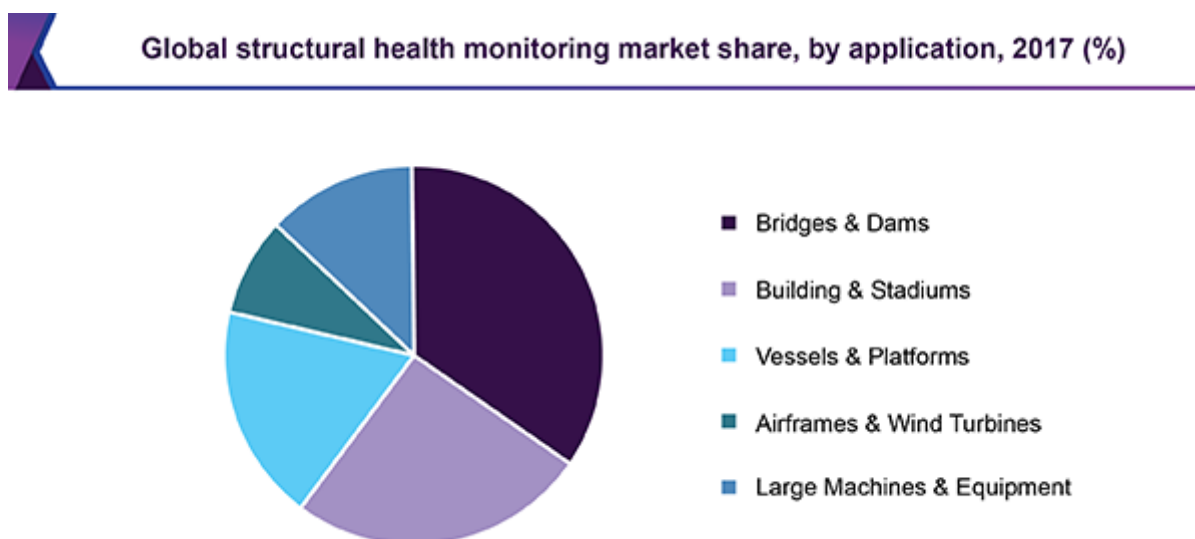


Figure 2: Global SHM Market Analysis for 2017 (Coherent Market Insight 2020)

Increasing government initiatives towards SHM system standardization and public safety are one of the contributing factors in the market growth over the years. The growing infrastructural development across the world and increasing awareness of impending dangers and natural

disasters are compelling governments worldwide to apply certain regulations regarding SHM. The recent cost, size, and various sensors such as vibration and load have been reduced significantly. Availability of these small and cost-effective sensors allow reduction in overall cost, which includes installation and additional material cost such as cables and other components. The increasing focus on low-cost energy harvesting systems and adoption of distributed optic fiber is also contributing to the growth of SHM. However, more work needs to be done in terms of cost reductions, because these sensors rely on heavy and sophisticated equipment to analyze the data obtained. Europe dominated the global structural health monitoring market in 2019, by about 32.8% share in terms of value, followed by North America (Coherent Market Insight 2020).

Additive Manufacturing

In recent years, additive manufacturing (AM) has become more mature and adopted in various applications. The importance of quality assurance cannot be overemphasized hence extensive research has been conducted on preserving the quality of additively manufactured parts. The additive manufacturing process produces parts by the deposition of the material layer by layer. When the melt pool of the preceding layer does not completely fuse with the next layer, it may lead to vacancy, thereby creating pockets between the layers. These defects may be undetected and subsequently lead to sudden failure or decrease in the lifespan of the material. The advancement in today's technology has shifted the manufacturing technique from a conventional approach to a more readily available method in 3D printing. The need to create lighter, stronger and more complex parts has been hailed as one of the greatest achievements of modern technology. While many companies and individuals moved towards the use of additive manufacturing technique because of its low cost and high performance, consideration must be made as well in terms of quality control. Additive manufactured parts are susceptible to defects such as cracks, surface

roughness and occurrence of porosities inside the final part. As 3D printing becomes mainstream for part fabrication from polymers and metals, there is a need for timesaving, cost-effective and readily available methods of monitoring this type of material to make sure it meets the required standard.

Composite Structures

Lightweight materials are in increasing demand in the manufacturing and automotive industries. Lighter products have been widely used in roofs, doors, floor segments, body panels, frame segments, battery access doors, and seating, having a weight saving of up to 60%. This has been shown to enable better performance, such as improving the fuel economy when used in the automotive industry (Koricho and Belingardi 2015). The use of lightweight structures in the aerospace industry has been credited to be one of the highest fuel economy friendly materials. High performance composites such as carbon-fiber reinforced plastics (CFRP) is one of the main materials currently used in the manufacturing of Airbus A350 and Boeing 787 Dreamliner, glass-fiber reinforced plastics (GFRP) sandwiched with phenolic resins are commonly used in the interior due to their low weight to stiffness ratio (Bachmann et al. 2018). Researchers have indicated that the structural efficiency of a structure depends on the reduction of density of the material (up to 400% more effective compared to increasing stiffness or strength). Along with aluminum alloys, CFRP is the most widely used aerospace structural material used, with over 40% of market share. This attribute lies in CFRP's high tensile strength, superior stiffness characteristics, light weight, strong resistance to chemicals and low thermal expansion, with the major applications being structural components of the wing box, fuselages, and stabilizers. Other advantages of composites are fatigue resistance, thermal and chemical resistance as well as the electrical insulation properties.

The quest for lightweight vehicle structures has been actualized with the use of composite materials, not only does it contribute to weight reduction, these fiber reinforced materials are resistant to corrosion, impact cushion, noise attenuation, and can also accommodate parts consolidation (Koricho and Belingardi 2015).

Since the primary concern in the aviation industry is safety, the lack of experience and confidence in the long-term performance and mechanical properties has made it limited in its usage. Many methods have been established to determine and analyze the effect of damage in a composite material. Since microscopic failure occurs before the ultimate failure of the test specimen on a macroscopic scale, it is uncertain if maximum values of stress-strain curves can be reliable in ascertaining relevant material properties.

Belingardi et al. (2013) performed an experiment to determine the damage zone of a GFRP using recorded video, digital microscope, and polariscope, with the result indicating that the tensile strength, crack initiation and propagations around are influenced by the quality of the notch. Due to the complexity of the structures of composite materials, failures of reinforced composites most often start on the microscopic scale and continue to grow before reaching a structurally perceptible level (Sause et al. 2016).

Camera Based Measurement

Cameras have been used to measure structures in different mechanical engineering applications. They provide a non-contact approach to structural health monitoring, unlike any other means of measurement, cameras are relatively cheaper and can make simultaneous full field measurements. Currently, high resolution and high-speed digital video cameras along with image analysis methods, such as 3D digital image correlation (3D DIC) are prevalent (Sarraf et al. 2018). Although 3D DIC provides smooth mode shapes with high accuracy, this method requires a

speckle pattern or high contrast markers mounted or painted on the surface of the structure (Raunio, Nieminen and Virtanen 2020). Edge detection algorithms have also been used in measuring displacement on simple structures. Phase based algorithms have recently gained traction over the past years mostly for structural motion estimation, and system dynamics identification (Chen, Buyukozturk and Nepf 2016). Phase-based motion estimation algorithm along with motion magnification algorithm one can obtain the resonant frequencies and mode shapes of several lab scale benchmark structures consisting of a cantilever beam and a pipe test specimen.

Some of the advantages of this measurement technique is the efficient use of a single camera, which produces an in-plane motion capture resulting in a lesser computational cost, absence of surface preparation methods before analysis, and an efficient algorithm capable of extracting the natural information of the structure under normal conditions (Serraffi and Mao 2019).

Thesis Structure

This thesis consists of 6 chapters. Following the introduction chapter, Chapter 2 presents the literature reviews and research done on additive manufacturing, composite materials, and defect detection mechanism used in lightweight structures, then delves into the research done on various video magnification techniques employed in the past. Chapter 3 presents the problem statement, the object of the research and the new idea. Chapter 4 presents the methodology used in carrying out the research, which involves video capturing, motion magnification, resonant frequency extraction of both the intact material and a defective material, and the process involved in obtaining the operational mode shapes of the test material and modal assurance criterion (MAC). Chapter 5 covers the results obtained from the experiment and comparing it with the results

obtained using the LDS, phase-based motion estimation and ANSYS simulation. Finally, Chapter 6 presents the conclusions and recommendations for future work.

CHAPTER 2

LITERATURE REVIEW

There has been a drastic improvement in manufacturing techniques of lightweight structures over the years, however, these techniques experience several metallurgical limitations.

Most additive manufactured (AM) parts are susceptible to porosity and void and thereby affecting the mechanical properties of the structure. These defects usually occur when the melt pool of the next layer does not completely fuse with the preceding layer thereby creating a series of pocket holes. Moreover, while most 3D printings are done in open spaces that increase the rate of gas porosity, even in a controlled environment there may still be traces of air finding its way to the metal. The repetitive layering of the powder leads to the formation and collapse of unbelted holes, resulting into the entrapment of gas thereby creating pocket holes.

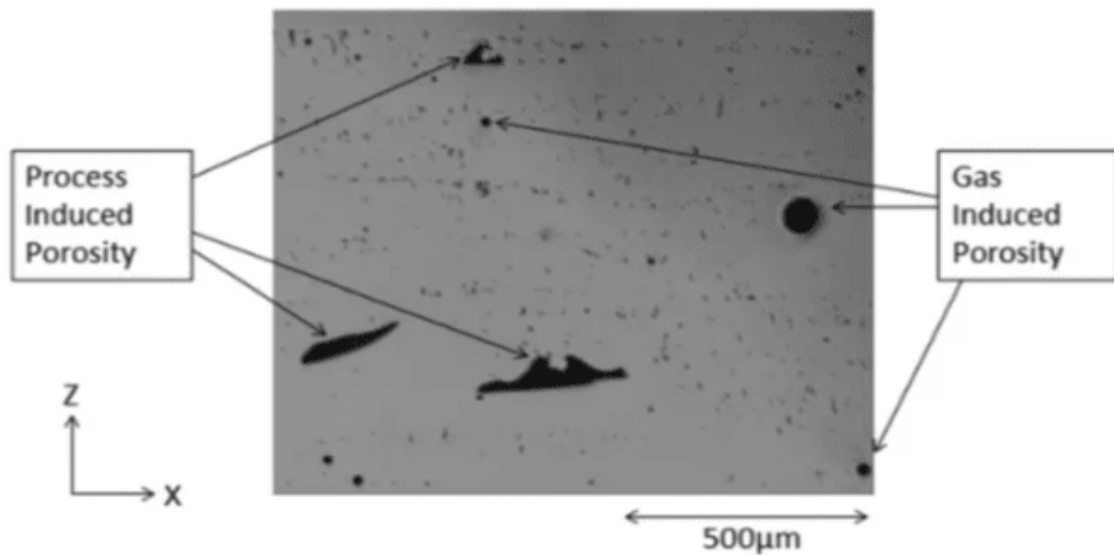


Figure 3: Defects in 3D Printing. (Molitch-Hou 2017)

Cracks can develop along grain boundaries owing to the temperature difference between the next layer and the preceding one and the tensile force from a partially melted zone. The AM process is prone to defects, which may be undetected if not carefully evaluated.

There have been various methods used for evaluating the structural integrity of lightweight materials. It has been shown that conventional destructive methods such as tensile, compression or hardness tests may cause more harm than good with higher material costs. Other non-destructive testing methods such as X-ray imaging, ultrasonic and eddy current scans may suffer from obtaining a reasonable result that requires the defective area to be known in advance and accessible to testing (Chong et al. 2015)

The Direct Image Correlation (DIC) is a 3D full-field non-contact optical technique to measure deformation, contour, vibration, and strain. It uses a stereoscopic sensor with each object pointing to a specific pixel in the direction of the image plane. Having the awareness of image parameter for each sensor and the orientation of the sensors with respect to each other, the position of each object point in three dimensions can be calculated (Strauss et al. 2017). This technique yields a quantitative measure of deformation occurring between two subsequently acquired images of an object under load.

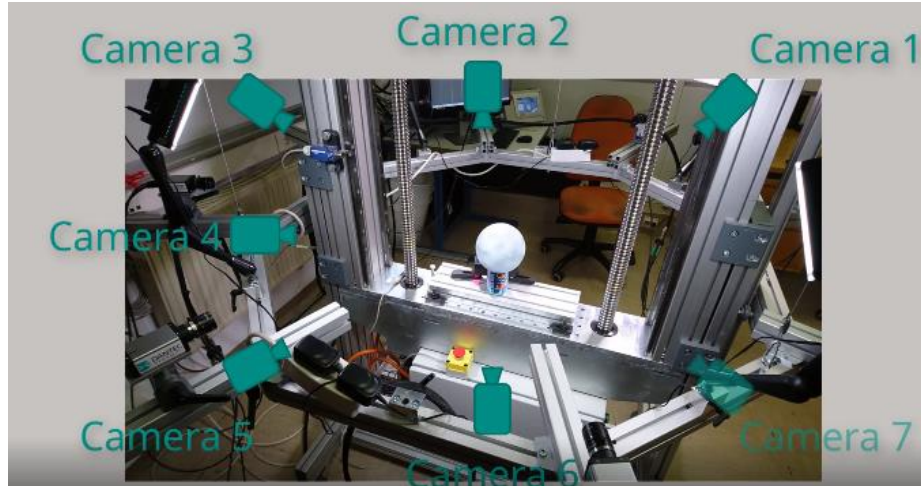


Figure 4: 3D-DIC System Demonstration (Dantec Dynamics n.d)

Although the DIC produces reasonably accurate and smooth pattern shapes, it needs more than one camera to collect data. To obtain the vibration characteristics of a sample, it needs more information from several matching calculations. Furthermore, the complex processes coupled with high computational costs and surface preparation have made it practically difficult to perform.

X-ray computed microtomography technique has been employed in detecting pores in AM parts. The sample is often rotated 360 degrees for X-ray examination from different angles. Then, the 2D gray images perpendicular to the vertical axis of the sample are obtained and stacked using a software to create a 3D view of the specimen (Slotwinski, Edward and Hebenstreit 2014). The realization of the three-dimensional view of the internal pores coupled with its non-destructive means gives it a critical advantage over other means of analysis. However, X-ray scanning requires higher resolution scanning to actualize an accurate result. Furthermore, conducting an X-ray scan can be very expensive and time consuming.

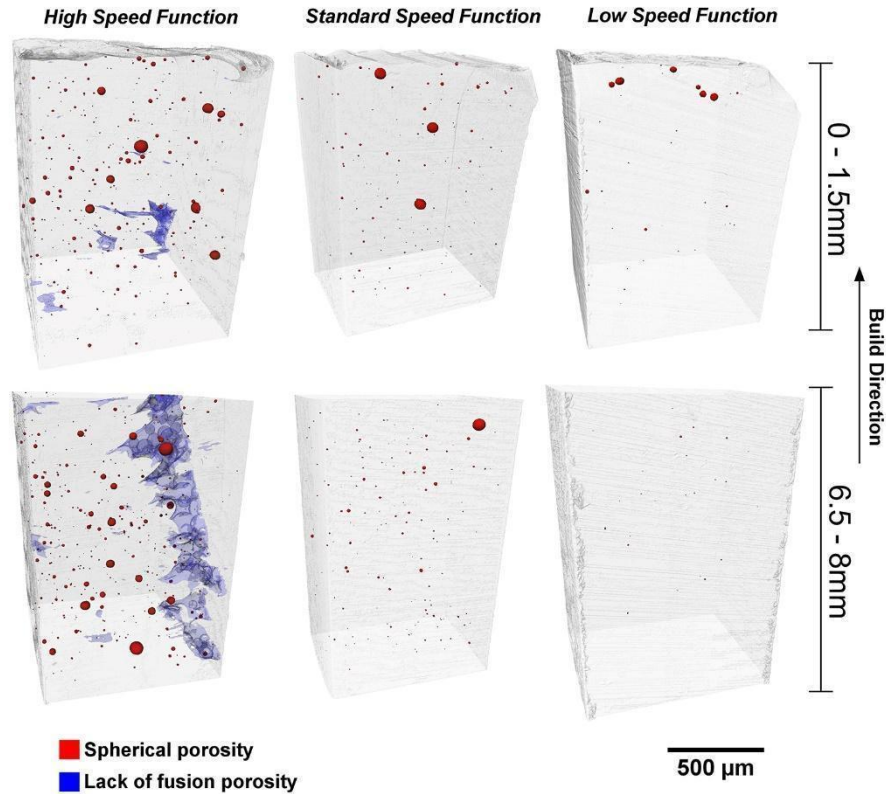


Figure 5: X-Ray Microtomography Showing Pores at Different Scan Speed (Koslow 2016)

Vibration has been an important factor in terms of measuring the service life of an equipment, since they can be applied in identifying system parameters, monitor the condition of operational equipment, predict, and diagnose failures in industrial equipment. The basic principle lies in the theory that damage exerts an effect on the physical properties of structure such as damping and stiffness and subsequently changes the modal properties. There are two kinds of methods used in vibration analysis: contact and non-contact methods.

A good example of the contact method is the impedance-based measurement. This method makes use of lead zirconate titanate (PZT) wafers as collocated sensors and actuators simultaneously excite the structure and measure its response. The impedance response identifies defects in the entire structure, which is hidden from the “line-of-sight” when using ultrasonic or

acoustic testing (Sturm et al. 2019). Another contact method commonly used is the accelerometers and Linear Variable Differential Transformer (LVDT) displacement sensors, which are usually placed on the test object to collect vibration data. However, the mass-loading effect is the limitation of the use of a contact-based sensors, which can affect the physical properties of the measured structure. Furthermore, these approaches cannot provide a full-field spatial resolution view but can only measure the corresponding signal of a single point (Peng, Zeng and Wang 2020).

The non-contact method such as the Laser Doppler Vibrometer (LDV) collects data from the response of structures without causing any mass loading effects or changing the structural stiffness of the measured material. However, LDV can only be used to obtain data from a single point. To obtain a high spatial resolution data, multiple LDV's will be utilized thereby making it relatively expensive when compared to video-based measurements (Serraffi and Mao 2019).

There are different types of video-based measurement methods. The early attempts to estimate motion fields from videos was made known by Lucas-Kenade and Horn-Schunck. These techniques are based on the optical flow image intensity algorithm. These methods have been used for detecting image discontinuities which can then be used to perform image segmentations based on the differences in successive image frames (Simon and Mathews 2004). The intensity-based optical flow has been widely used in vibration measurement of structures. However, its sensitivity to noise and disturbances has made it susceptible to errors.

Current methods utilize the phase-based optical flow approach to estimate the motion according to the phase difference of the image. The phase information of the image provides robust performance with respect to the variations of image intensity. For a low amplitude sub-pixel motion, the effect of signal extraction can be significantly improved by denoising the phase signal.

The phase-based approach can extract the motion by taking into consideration of the phase variations instead of manipulating the raw pixel intensity values.

Cong Peng et al. (2020) performed a camera-based vibration measurement on a lightweight structure by extracting the phase-based displacement without calculating the optical flow vectors and phase gradient. The extracted displacement was used to compute the vibration signals in the time domain and frequency domain. This was inspired by the Fourier transform theorem, which indicates that motion in the spatial domain leads to the phase variation in the frequency domain. Because localization of analysis is impossible for the Fourier transform, the Gabor transform is introduced. The Gabor transform is generated based on the simulation of the human visual system. Using the features of direction and frequency selectivity of a Gabor filter, the local amplitude and local phase in various directions can be extracted and analyzed. Then the displacement signals are obtained according to the relationship between local phase and displacement. This technique utilized a high-speed camera to capture sequences of images. Furthermore, the experiment was conducted with the use of an accelerometer for verification leading to the effect of mass loading.

Phase-based motion magnification technique is the new method for structural monitoring because it provides non-contact, real-time, high-dimensional signals. The color changes in a human because of blood flow have been used by researchers in the biomedical optics field to find biomarkers such as heart rates. The same approach can be used for detecting spatial-temporal changes in lightweight structures, since the changes in phase and amplitude identified by a camera can be correlated to the structural change in the system. To accurately estimate the structural change of the system, a comparison needs to be carried out between the two systems where one will be assumed to be the baseline in an uncompromised condition.

The phase-based motion magnification process involves the comparison of image sequences between the uncompromised and compromised parts, where the difference in the spatial domain will lead to a proportional change in the phase. This entails that motion magnification within a selected frequency band corresponding to the natural frequencies of the target structure will preserve their original motion information by preserving the phase variations within the same band (Prakash et al. 2020)

Neal Wadhwa et al. (2017) performed a motion magnification by leveraging the theory that local phase differences can be used to manipulate local motions. This was done by taking an image and projecting each image frame onto a complex steerable pyramid and then independently amplifying the phase differences between all corresponding basis elements. This is almost like the linear amplification method except that the amplification factor involved is the phase difference instead of intensity changes. The signal-to-noise ratio is improved by temporally and spatially filtering the variations to remove components that correspond to noise and keep those that correspond to signal. The filtering also gives a way to isolate a signal of interest as different motions often occur at different temporal frequencies.

CHAPTER 3

PROBLEM STATEMENT AND RESEARCH OBJECTIVE

Problem Statement

While a laser can measure vibrations without the effect of mass loading, it can only measure a single point, unless there are multiple sensors or a sophisticated scanning/analyzing algorithm to assess the whole structure, which are generally expensive and require a considerable amount of time to obtain the results. The use of LDV may not be practical due to its ineffective frequency range for measuring structures with very large displacements or displacements in low frequency.

Research Objective and New Idea

The objective of this research is to accurately and reliably detect and identify the damage characteristics of lightweight mission-critical parts in its early stages. In order to accomplish this goal, this research proposes to utilize the vibration characteristics of the structure by exploiting the phase-based motion estimation and magnification technique. This technique is a non-contact approach that utilizes a high-speed digital camera to capture the vibration of the structure. By applying a temporal filter, the video signal will be spatially decomposed to extract the local phase and amplitude information of the images. Current non-contact sensors rely on the collection of data at a single point of the test specimen. The advantage of using a video-based approach is that one can collect data of the whole structure at once. This method is much easier to set up than having multiple laser sensors in different locations or placing multiple contact sensors all over the structure.

This paper proposes the use of a video camera to record the displacements of the structure from a sequence of images. By utilizing the motion estimation algorithm, the natural frequencies

of the subject will be extracted. Utilizing the motion amplification algorithm, the operational mode shapes of the subtle motion will be magnified and compared to the baseline mode shape to estimate the health of the structure. This experiment is based on a hypothesis that a defect in a structure will lead to a reduction in the dynamic stiffness of the material and an increase in damping, thereby causing a change in the natural frequency of the structure.

Considering the prior advancements in utilizing video magnifications to detect hidden changes in color, heartbeat, and vibrations, this study will utilize video magnification for fault detection on 3D printed materials, which has not been fully explored. The process is based on damage identification from subtle vibration and the amplification of this vibration to make it easier to detect and analyze the structure. Vibration of a material provides information on the modal properties of that material such as the natural frequency, this obtained natural frequency can be further used in analyzing the properties of this material and the precise defect information can be obtained.

CHAPTER 4

METHODOLOGY

Experimental Overview

The first objective of this experiment is to verify the use of video-based motion estimation methods in structural health monitoring of AM systems. This is done by printing a healthy or intact AM test part. The displacement of a test sample is measured by a laser displacement sensor and a high-speed camera. The sensitivity and accuracy of the video-based method is then compared to that of the laser displacement sensor.

The second objective is to use a video-based method to investigate the resolution of defects. To accomplish this, different samples with an increasing defect size were manufactured to simulate varying degrees of defect, and the vibration responses are measured. This experiment was also carried out on samples with different defect locations while having the same size of defect. The natural frequencies of the defective sample along with the mode shapes were compared with the baseline to determine the extent of the damage.

Lastly, the video-based motion estimation was utilized to detect the defects in a composite material. This was accomplished by fabricating two different composite materials. The mode shapes of defected sample and its resonant frequencies are compared to those of the baseline to detect the smallest detectable defect.

Equipment and Experimental Setup

The experiment required the use of MATLAB software on a desktop computer with at least 8GB of RAM to run the motion magnification code, which magnifies the small motion obtained from the vibrating body. The experimental setup includes a Tiertime Cetus MK3 3D printer,

desktop computer, high-speed digital camera (Chronos 1.4), a laser displacement sensor (ILD 1420), and room lighting. The process was conducted using known 3D printed structures such as PLA beams and composite materials like GFRP and fiber glass.

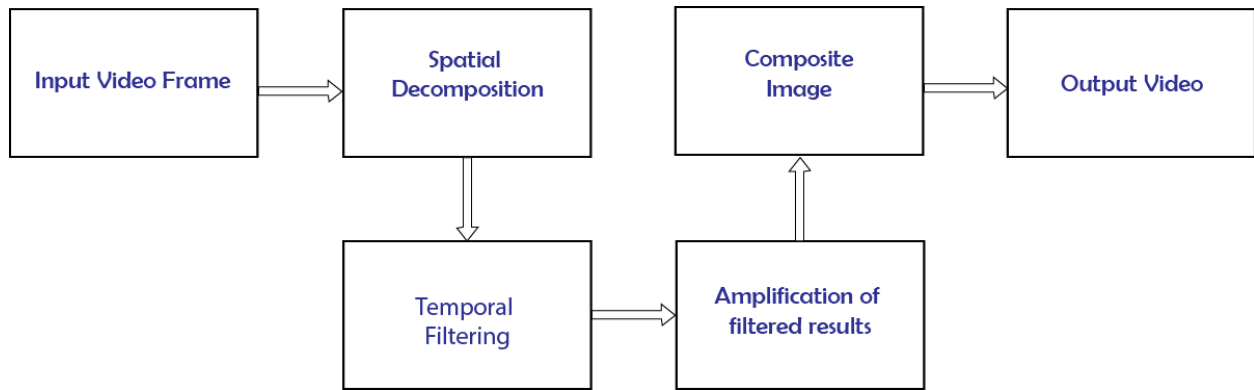


Figure 6: Schematic Diagram of the Video Magnification process

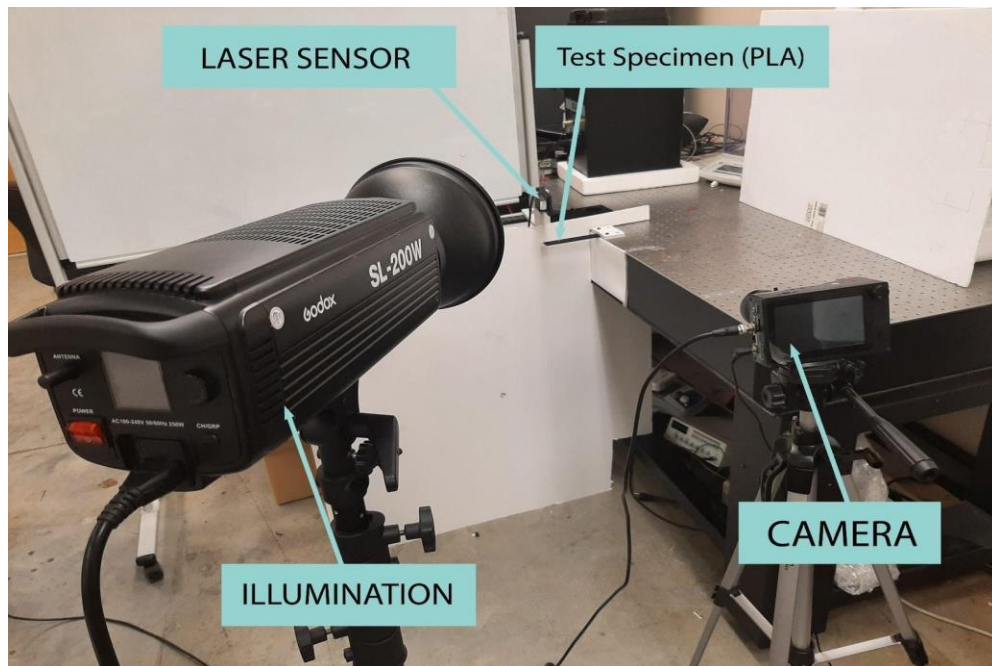


Figure 7: Experimental Setup

To conduct the experiment, the equipment was set up as depicted in Figure 7. A CHRONOS 1.4 high-speed camera equipped with a maximum processing rate of 1.4 Gigapixel per second, 1.3-megapixel image sensor, and a 12mm zoom lens are utilized to capture the sequence images at 3270 frames per second (fps). The duration of the measurement is 1 second which provides a total of 3270 frames. The resolution was set at 1280 x 330 to capture the entire length of the beam. The distance between the camera and the beam was approximately 1.2192 meters, enabling the camera to capture the full length of the test sample within its field of view. The video-based test and the laser sensor displacement test were performed simultaneously on the beam.

Material Selection

The beam sample was manufactured with Polylactide (PLA), having a dimension of 25 mm width, 150mm length and a thickness of 3mm. The shape was designed in the form of a cantilever beam which is a common element of civil and mechanical engineering structures (Belendez et al. 2005). The parts were printed using a Tiertime Cetus MK3 3D printer with a layer height of 0.1mm and a fill density of 99 %. The same material was used for creating the supporting structures as well.

Table 1: Material Dimension of PLA

A	Clear Span	130mm
B	Centre Length	140mm
C	Overall Length	150 mm
D	Width	25mm
E	Thickness	3mm

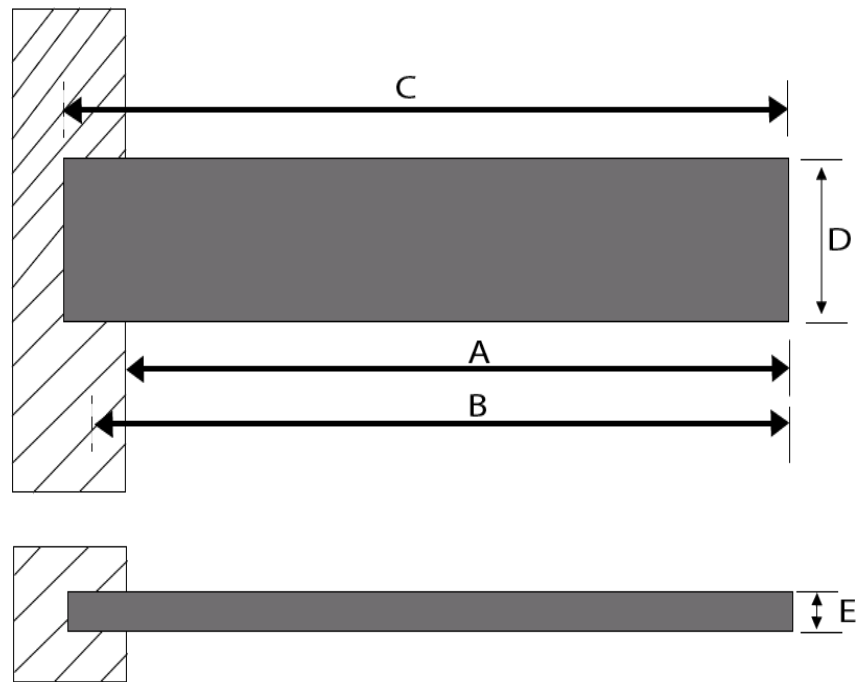


Figure 8: Schematics of the Experimental Sample Dimension

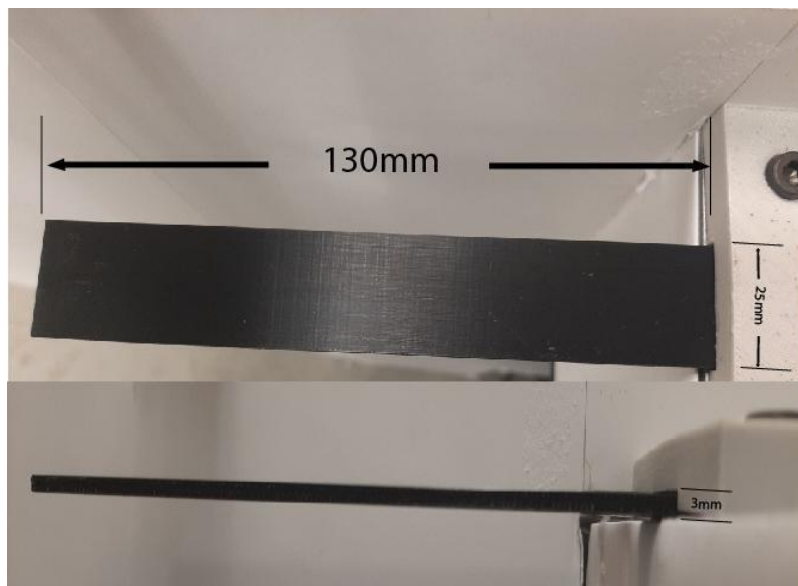


Figure 9: Experimental Setup showing the Dimension of the Sample

Additive Manufacturing of PLA

Additive manufacturing, which is the process of joining materials to make desired parts, is usually performed layer by layer, which is different from the conventional method of manufacturing that is subtractive. The proposed model was designed using SolidWorks and exported to a Tiertime Cetus MK3 3D printer to fabricate using a PLA plastic. PLA is a vegetable-based plastic material that is a biodegradable thermoplastic aliphatic polyester often used in additive manufacturing. PLA has been used in many product developments due to its usefulness in rapid prototyping. The ability to be mixed with other polymers contributes to its varying usage, and its characteristics such as heat resistance, stiffness, smooth surface finish, ability to be molded into different shapes have made it useful for product design and prototyping.

Model Design and Fabrication

The model was designed using SolidWorks. Five samples of the healthy beam are converted to STL format. This design model is laid out in Figure 9, which was then converted to Geometric Code (G-code) by a slicing software, Tiertime UpStudio. The PLA beams having a dimension of 3 mm thick, 150 mm long, and 25 mm wide and were fabricated with an extruder nozzle temperature of 220° C.

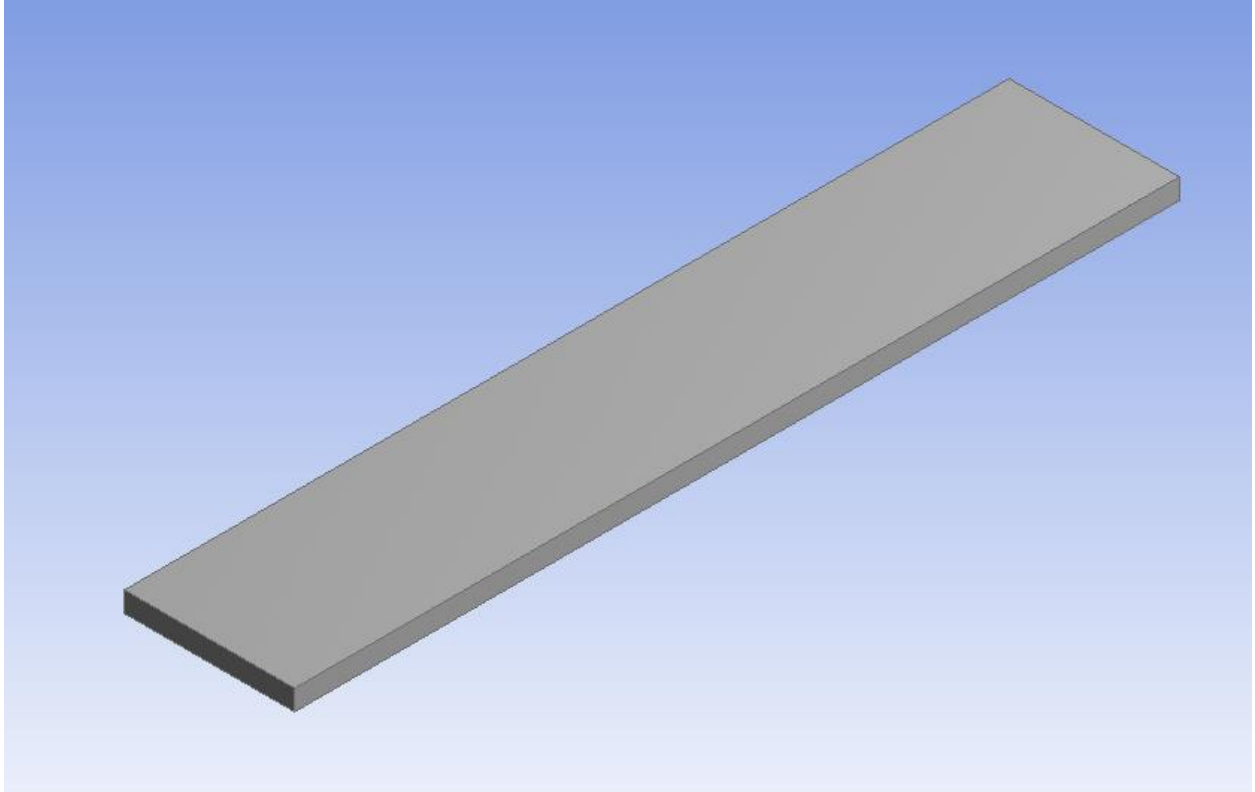


Figure 10: 3D Model of a PLA Beam

Testing using Laser Displacement Sensor

The micro-epsilon optoNCDT 1420-100 laser displacement sensor (LDS) was used to measure the displacement of a particular position. The LDS works based on the principle of optical triangulation. The movement of the object causes the change in the laser reflection, thereby making it possible to detect displacements.

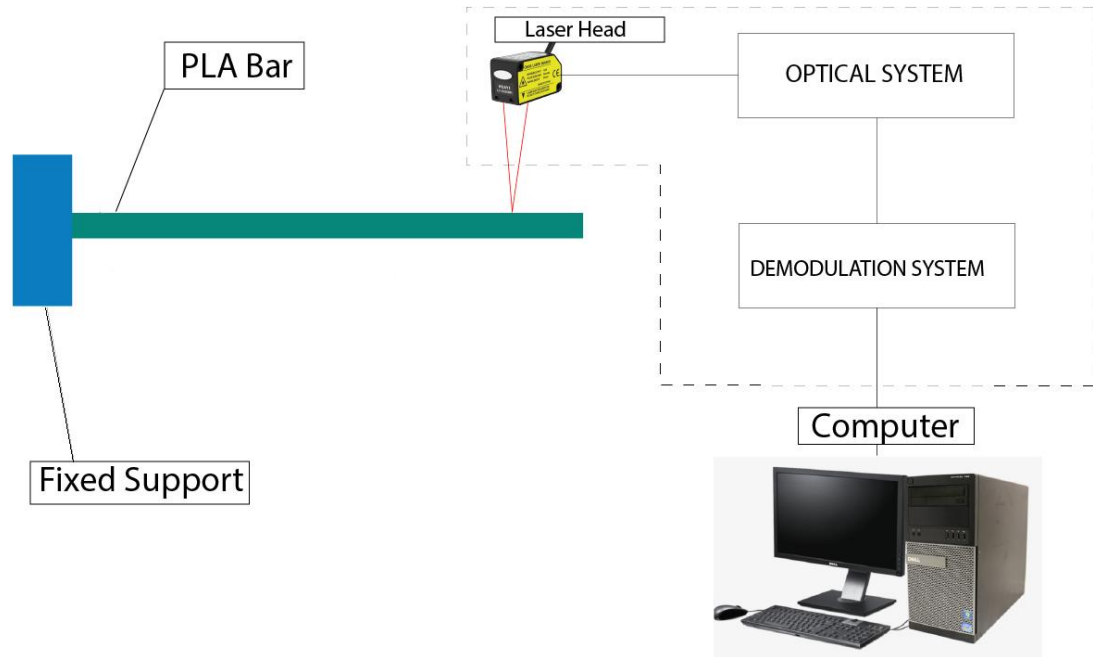


Figure 11: Schematic Layout of a Laser Displacement Sensor

Phase Based Approach

The phase-based motion extraction method was inspired by the Fourier transform shift theorem, which indicates that motion in the spatial domain leads to the phase change in the frequency domain. The input source video from a high-speed camera of a vibrating structure is processed using complex linear filters to identify amplitude and phase variations for each frame of the video. The phase signals in time, which are representations of motion of pixels with good edges or local contrast, are processed into displacement measurements.

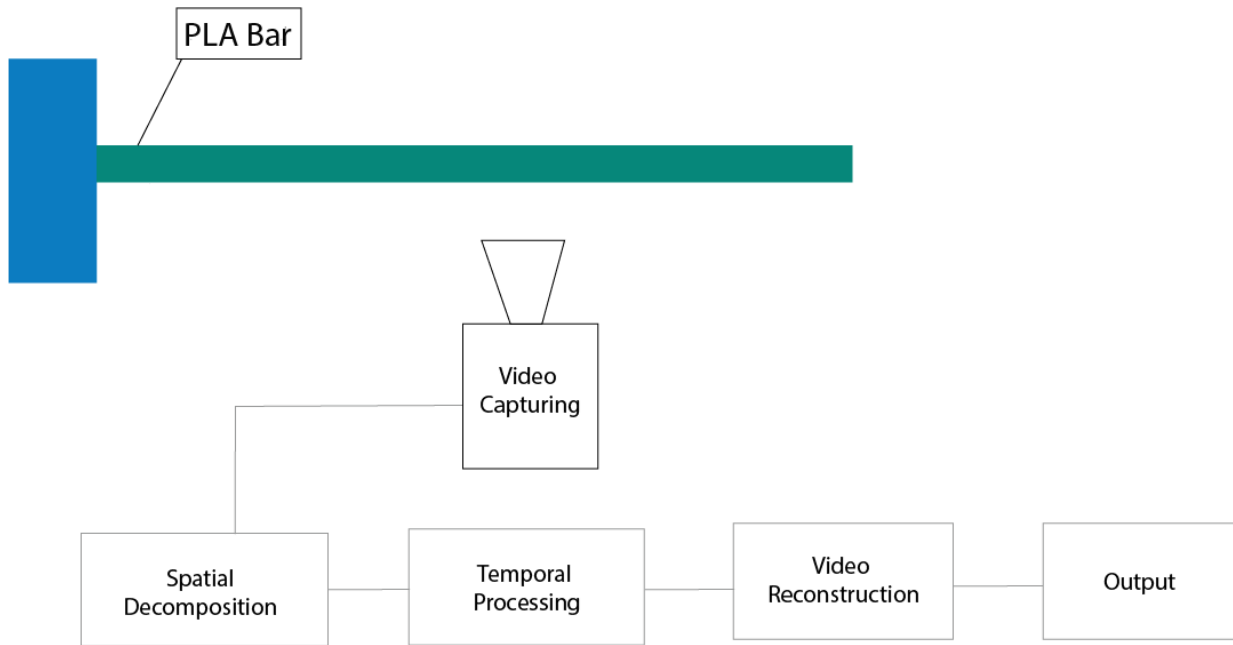


Figure 12: Schematic Layout of the Phase Based Motion Estimation Process

For signals such as the spatial domain representation, there is a frequency domain representation that is commonly used to decompose signals using the Fourier transform. However, the Fourier transform only reflects the overall characteristics of the signal. Thus, the phase and the amplitude of the Fourier transform correspond to the position and intensity of global motion. A Gabor filter, which is a sinusoidal wave multiplied by a Gaussian function, introduces locality to the Fourier series causing the Fourier coefficients to be calculated for a signal in a local amplitude and local phase representation. Using the Gabor filter, the video can be decomposed into local amplitude and phase. Local phase signals have been demonstrated to correspond to motion signals in a video, and this is how the motion signals can be obtained from the video.

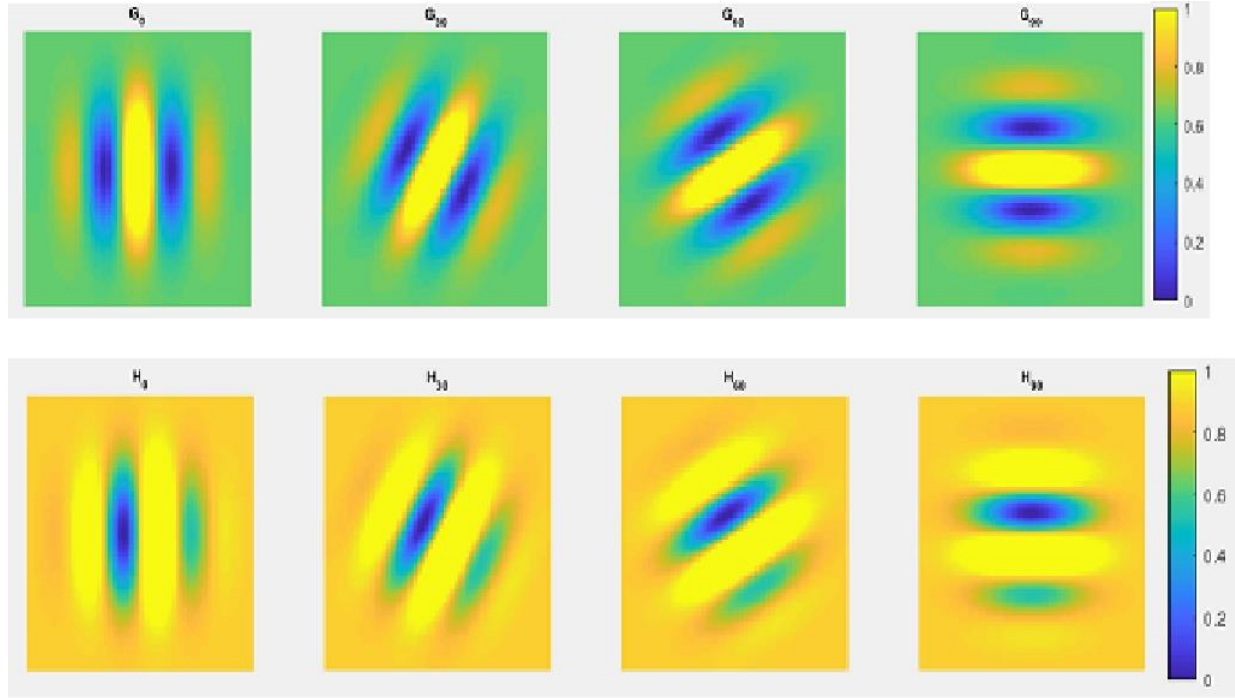


Figure 13: Complex Gabor Wavelets with 4 Orientations Different Orientation for both Real and Imaginary

The 2D Gabor function can be expressed as:

$$I(x, y; \lambda, \theta, \psi, \sigma, \gamma) = \exp\left(-\frac{x'^2 + \gamma^2 y'^2}{2\sigma^2}\right) \exp\left(i\left(2\pi\frac{x'}{\lambda} + \psi\right)\right) \quad (1)$$

where $x' = x\cos\theta + y\sin\theta$ and $y' = -x\sin\theta + y\cos\theta$.

In Eq. (1), x and y are the independent variables and θ determines the orientation of the Gabor wavelet. Zero degree corresponds to vertical position while 90° correspond to horizontal position. Here λ represents the wavelength of the sinusoidal component. Increasing the wavelength produces a thicker stripe and decreasing the wavelength produces a thinner stripe. σ represents the standard deviation of the Gaussian envelope which determines the size of the acceptable region of the Gabor filter kernel. For a larger bandwidth, the envelope increases allowing more stripes. γ represents the spatial aspect ratio which determines the skewness of the Gabor Wavelet. ψ is the phase offset of the sinusoidal function.

The 2D Gabor function can also be represented as a simpler form of the real and an imaginary part:

Real

$$g(x, y; \lambda, \theta, \psi, \sigma, \gamma) = \exp\left(-\frac{x'^2 + \gamma^2 y'^2}{2\sigma^2}\right) \cos\left(2\pi\frac{x'}{\lambda} + \psi\right) \quad (2)$$

Imaginary

$$h(x, y; \lambda, \theta, \psi, \sigma, \gamma) = \exp\left(-\frac{x'^2 + \gamma^2 y'^2}{2\sigma^2}\right) \sin\left(2\pi\frac{x'}{\lambda} + \psi\right) \quad (3)$$

using the features of direction and frequency selectivity of Gabor filters, the local amplitude and local phase in different directions can be extracted (Peng, Zeng and Wang 2020). For a video with image intensity sequences $I(x, y, t)$ at a specific time t_0 and location (x, y) at time $t + dt$, the motion $(\delta x, \delta y)$ will be the applied intensity function. Therefore, the image intensity for the next time step is given as $I(x + dx, y + dy, t + dt)$. Using the convolution integral operation with the 2D Gabor wavelets, the image intensity $I(x, y, t)$ is transformed into a frequency domain $F(x, y, t)$

$$F(x, y, t) = I(x, y, t) \otimes g(x, y; \lambda, \theta, \psi, \sigma, \gamma) \quad (4)$$

This can be calculated by the integral,

$$F(x, y, t) = \int_{-\infty}^{+\infty} \int_{-\infty}^{+\infty} I(u, v, t) g(x-u, y-v; \lambda, \theta, \psi, \sigma, \gamma) dx dy \quad (5)$$

in the transformation described in equation (5) the integration is performed on x and y , x and y can be considered as dummy variables, which will disappear after the integration and the output of the transformation is only a function of u and v . The transformation will map the image intensities at each frame $I(x, y, t)$ to a new domain $G(u, v, t)$, with respect to u and v .

$$G(u, v, t) = F(x, y, t) \quad (6)$$

For example, let the Gabor wavelet with $\theta=0$ be convolved with image intensities at two consecutive frames, the transformation can be obtained as:

$$G(u,v,t) = \int_{-\infty}^{+\infty} \int_{-\infty}^{+\infty} I(x,y,t) \exp\left(-\frac{(x-u)^2 + y^2(y-v)^2}{2\sigma^2}\right) \exp\left(i\left(2\pi\frac{x-u}{\lambda} + \psi\right)\right) dx dy \quad (7)$$

Considering the motion of frame for image intensity of $t + dt$ for equation (7) yields:

$$G(u,v,t+dt) = \int_{-\infty}^{+\infty} \int_{-\infty}^{+\infty} I(x+dx,y+dy,t+dt) \exp\left(-\frac{(x-u-dx)^2 + y^2(y-v-dy)^2}{2\sigma^2}\right) \exp\left(i\left(2\pi\frac{x-u-dx}{\lambda} + \psi\right)\right) dx dy \quad (8)$$

By comparing equations (7) and (8), the phase values of complex coefficients in both frames $G(u, v, t)$ and $G(u, v, t+dt)$ may be extracted with ϕ representing the phase value of the complex number resulting from computing the definite integrals.

$$(u, v, t) = 2\pi\frac{u}{\lambda} + \phi \quad (9)$$

$$(u,v,t+dt) = 2\pi\frac{u+dx}{\lambda} + \phi \quad (10)$$

It can be shown that the phase difference in two consecutive frames is proportional to the motion, and the motion information is preserved in phase variations.

$$\Delta(u, v) = \phi(u, v, t) - \phi(u, v, t+dt) = 2\pi\frac{dx}{\lambda} \quad (11)$$

$$\Delta(u, v) = h dx \quad (12)$$

where h is a constant coefficient which is equal to $\frac{2\pi}{\lambda}$. dx is obtained via proportion to the temporal phase differences. Also, the motion in the y direction will be estimated by changing the orientation of the Gabor filter to $\theta = \frac{\pi}{2}$. Altering other orientation for the Gabor filter will also enable the algorithm to estimate the absolute projected motion in that direction.

Phase-Based Motion Magnification Process

Video motion magnifications could be utilized as a motion microscope for revealing imperceptible signals by naked human eyes. The basic principle involves the extraction of signals in the form of motion of a vibrating object from a video and the video decomposition into local

spatial amplitude and phase using a complex-valued steerable pyramid filter bank. The local spatial phase signals are temporally decomposed into a series of sinusoids representing harmonic motion. The phase signals are then temporally bandpass-filtered, amplified, and recombined back to form a motion magnified video. The resultant output video has the magnification of the motion in a specified band of temporal frequencies.

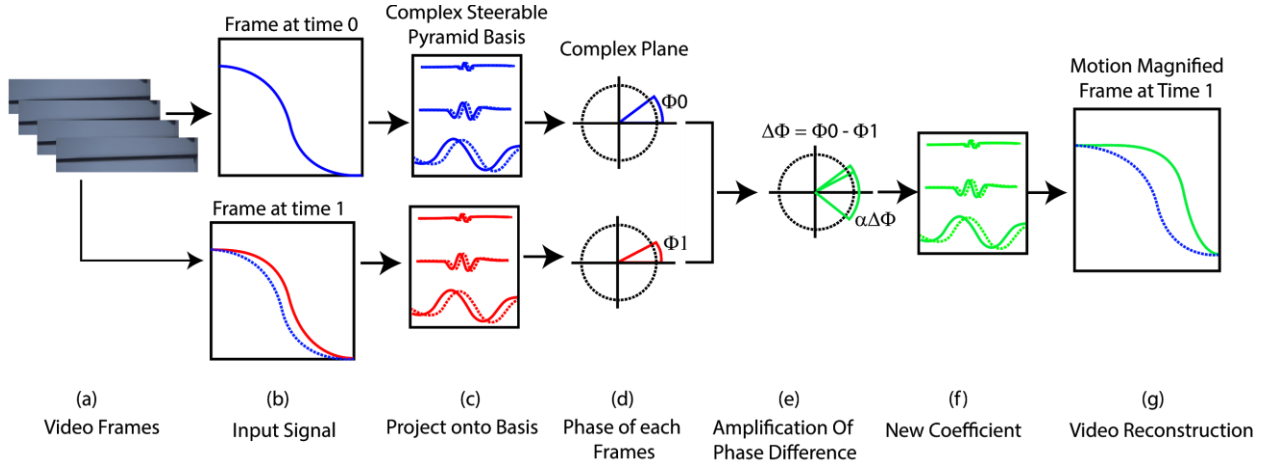


Figure 14: Schematic Representation of Phase-Based Motion Magnification

Motion can be represented in phase variations. Once again the intensities image sequences $I(x, t)$ given as $f(x)$ can be decomposed into a sum of sinusoids over all frequencies w using Fourier transform

$$F(x) = \sum A_w e^{i\phi^w} e^{-iwx} \quad (14)$$

With the displacement of the intensity I , the Fourier transform is given by a phase shift by $w\delta(t)$:

$$f(x + \delta(t)) = \sum A_w e^{i(\phi^w + w\delta(t))} e^{-iwx} \quad (15)$$

where the global phase information at frequency w for the displacement $\phi^w + w(t)$. Subtracting the phase at time 0 and t , we get the phase difference

$$e^{i\phi^{w+(1+\alpha)w\delta(t)}} \quad (16)$$

Performing the amplification of the phase difference by a factor α and using it to shift the Fourier coefficients of $I(x, t)$ yields.

$$\sum A_w e^{i\phi_w + (1+\alpha)w\delta(t)} e^{-iwx} = f(x - (i+\alpha)\delta(t)) \quad (17)$$

The amplification of the phase difference rather than the pixel intensity enables the algorithm to support large amplification factors and does not amplify noise.

Numerical Analysis

A 3D CAD model was created using the design modeler tool and analyzed using the model tool in ANSYS Workbench R2. The ANSYS Workbench is capable of simulating interactions of structural integrity, fluid dynamics, thermal analysis, topological optimization, harmonic response and many other engineering analyses. In this study, the modal analysis and the harmonic response of the beam were utilized to validate the experimental results.

The structure was designed with the specifications used in designing the experimental 3D printed object. Modal analysis was performed by constraining one end of the bar with a fixed support as depicted in Figure 15.

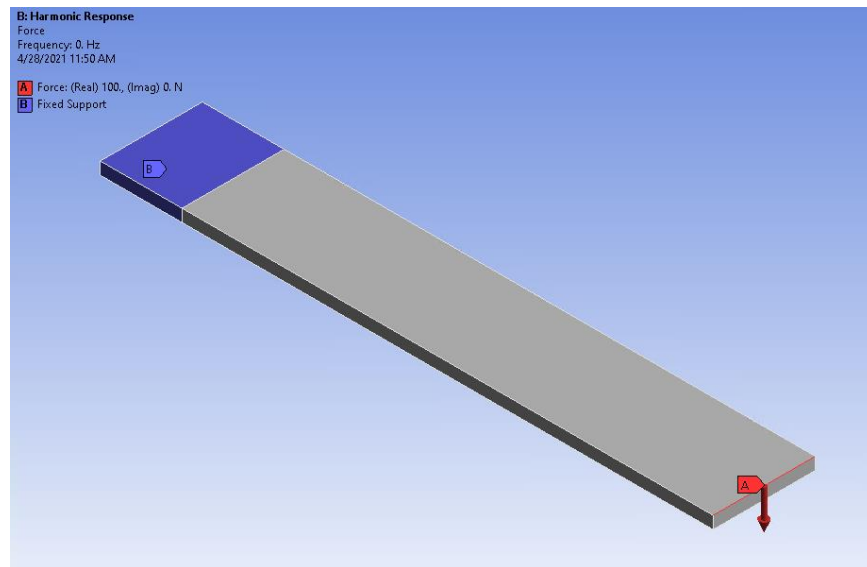


Figure 15: 3D PLA Model Showing the Fixed Support and Applied Force at the Edge

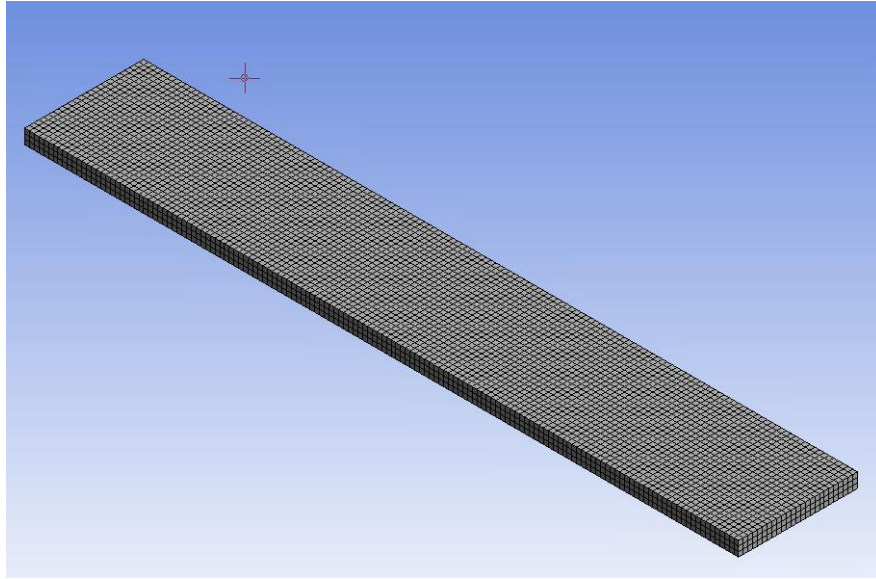


Figure 16: 3D PLA Model Mesh Selection

To evaluate the result, a solid quadrilateral (SOLID186 and SURF156) mesh element was used for this analysis with a finite element size of 1mm. To obtain the mode shapes of the beam, a fixed support was added to the split face. The maximum number of modes selected from the analysis settings was six. The total deformations were generated from the mode shapes using the modal analysis. The frequency response obtained after solving the analysis is used to create the mode shapes, which depends on the selected material (PLA) and the geometry. For SOLID186 the number of elements is 11250, while SURF156 has several elements of 25. For the harmonic response, a fixed support was added in the same spot as that of the modal analysis and a force of 100 N was applied on the free end to simulate the free vibration. This process was repeated for the damage cases as well.

Modal Assurance Criterion (MAC)

The modal assurance criterion is mainly utilized to estimate the rate of consistency (degree of linearity) between values of a modal vector. They act as a supporting factor in measuring the

confidence of a modal vector. Comparing modal vectors from different sources is made easier using the MAC. The experimental modal vectors obtained from the operational mode shapes can be easily compared with that from the finite element analysis. In this experiment, the modal vectors are estimated and compared with the theoretical vector to ascertain the degree of linearity and consistency of the different approaches used.

$$\text{MAC} = \frac{|\Psi_{dr}^T \{\Psi_{cr}\}|^2}{\{\Psi_{cr}\}^T \{\Psi_{cr}^*\} \{\Psi_{dr}\}^T \{\Psi_{dr}^*\}} \quad (18)$$

The modal assurance criterion takes on a value from zero, which means the result is not consistent, to one, which represents a completely consistent correspondence.

CHAPTER 5

RESULTS AND ANALYSIS

Resonant Frequency Measurements

The displacement signals from the video were first extracted, and then each of the individual signals were converted into a frequency domain using the Fast Fourier transform (FFT). The frequency responses are then averaged to get a single reliable frequency spectrum. Since not all pixels in the video may belong to a vibrating object, pixels with strong edges in the background were preferentially weighted. We can calculate the skewness of the distribution of the magnitudes of the frequency spectrum per pixel to only consider pixels with positive skewness above a certain threshold (Figure 17 and 18).



Figure 17: Original Image from the Video

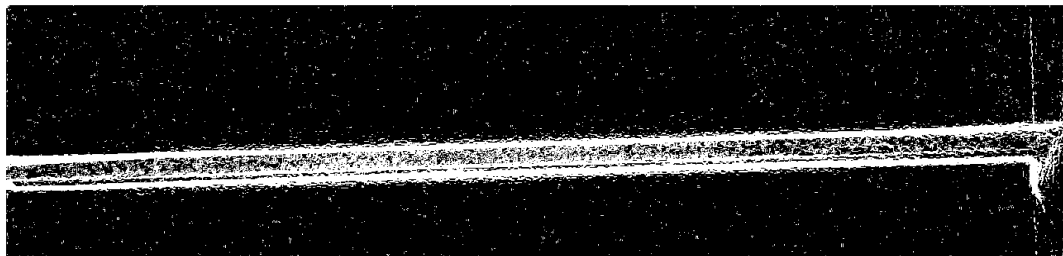


Figure 18: Mask Showing Pixels from the Image

To verify the consistency of the result, five samples of PLA were manufactured with the same dimension and physical properties within the 3d printer's tolerance. The samples were weighed using a smart weight dual digital scale to confirm the consistency of the manufacturing process, the result of the obtained mass is listed in Table 2. The average weight of the beam was calculated to be 12.804 g with a standard deviation of 0.00548.

Table 2: Mass of the PLA Samples

Samples	Weight (g)
1	12.80
2	12.81
3	12.80
4	12.81
5	12.80
STD	0.005477
Average	12.804

To identify the frequencies of interest a peak finding function was utilized, which is typically used for resonant frequency extraction. These extracted frequencies can then serve as the center frequencies during the motion magnification process. Table 3 summarizes the peak frequencies generated from the five samples. The average peak frequencies occurred at 39.04 Hz, 246.26 Hz, 409.81 Hz and 689.84 Hz, and the standard deviation obtained are 0.16, 1.30, 1.52 and 3.61, respectively. The results indicate that the peak frequencies are in harmony with each other.

Table 3: Frequencies Extracted using Phase-based Approach

	Mode 1 (Hz)	Mode 2 (Hz)	Mode 3 (Hz)	Mode 4 (Hz)
Sample 1	38.88	246.79	409.07	691.36
Sample 2	39.06	244.09	408.12	683.46
Sample 3	39.28	246.04	409.37	690.56
Sample 4	39.04	247.27	412.11	691.91
Sample 5	38.93	247.11	410.36	691.91
Average	39.04	246.26	409.81	689.84
Standard deviation	0.16	1.30	1.52	3.61

The vibration signal of the beam contains multiple frequency components along with noise, in which down sampling was utilized to extract the useful frequency components and remove unimportant components. The video resolution captured using the high-speed camera was 1280 x 330. After trimming the boundaries, the resolution became 1280 x 275, which was performed to reduce noise. To further eliminate noise, the magnitude of the image derivatives was obtained from the original frame, and the top 50% pixels of the largest derivatives were selected. A masking threshold was set from the mean value of these selected derivatives. The pixel with better texture (i.e., with gradient values above the threshold) was used to perform the FFT (Figure 16).



Figure 19: Mask showing Pixels with extracted displacement using the mean threshold

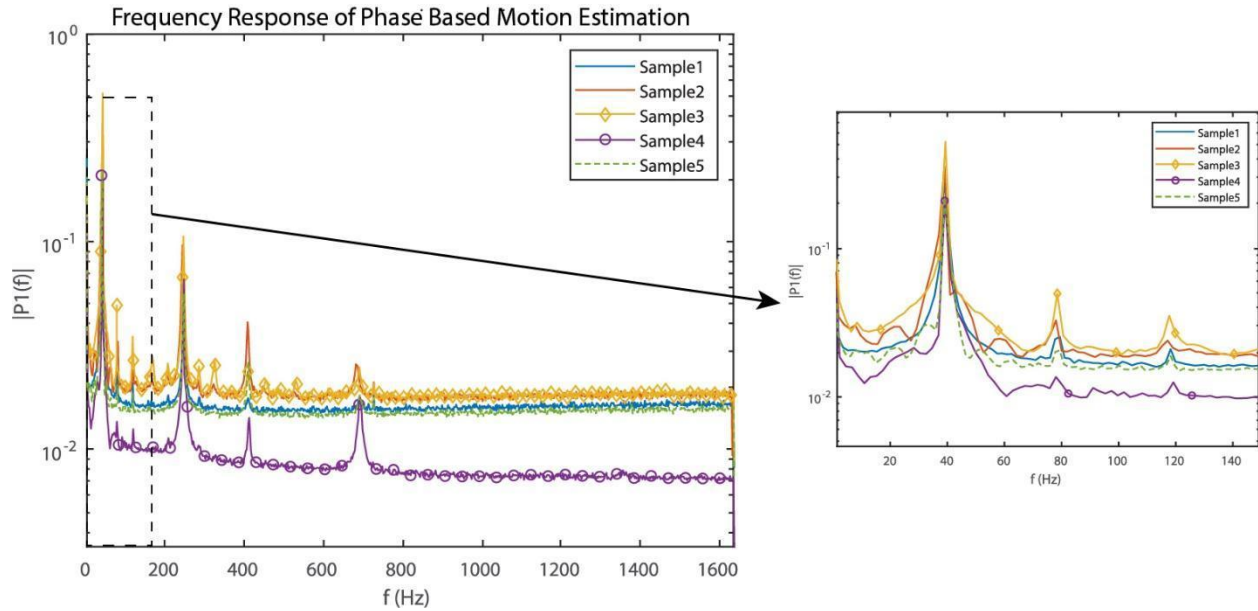


Figure 20: Resonant Frequencies of PLA Samples

Validation of the Phase-based Measurements

To validate the results obtained using the phase-based method, the displacement of the healthy PLA beam (baseline) was obtained using the LDS at the same time. The natural frequencies extracted from the LDS data were then compared to those obtained by using the phase-based method. The use of LDS ensured that there was no mass loading effect due to its non-contact nature. The frequencies obtained from the phase-based method was compared with the LDS method in Figure 21 and the results are listed in Table 4.

Table 4: Frequency Comparison between LDS and Phase-based Approach

	Mode 1	Mode2	Mode3	Mode4
Laser	39.5	247.375	405.25	691.5
Phase-based	39.04	247.27	412.11	691.91
STD	0.32	0.07	4.85	0.29
Error	0.46	0.11	6.86	0.41
Percentage Error (%)	1.16	0.04	1.69	0.06

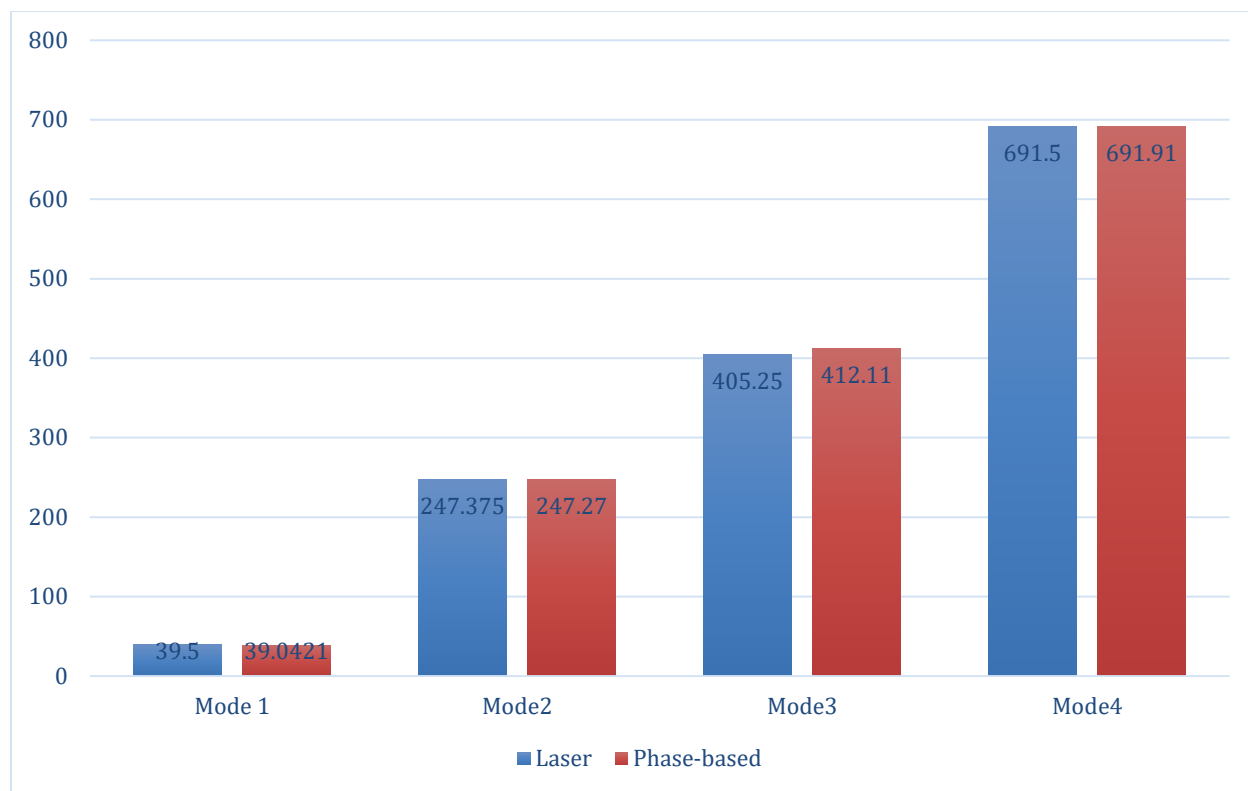


Figure 21: Resonant Frequencies Comparison of LDS with Phase-based Motion Estimation

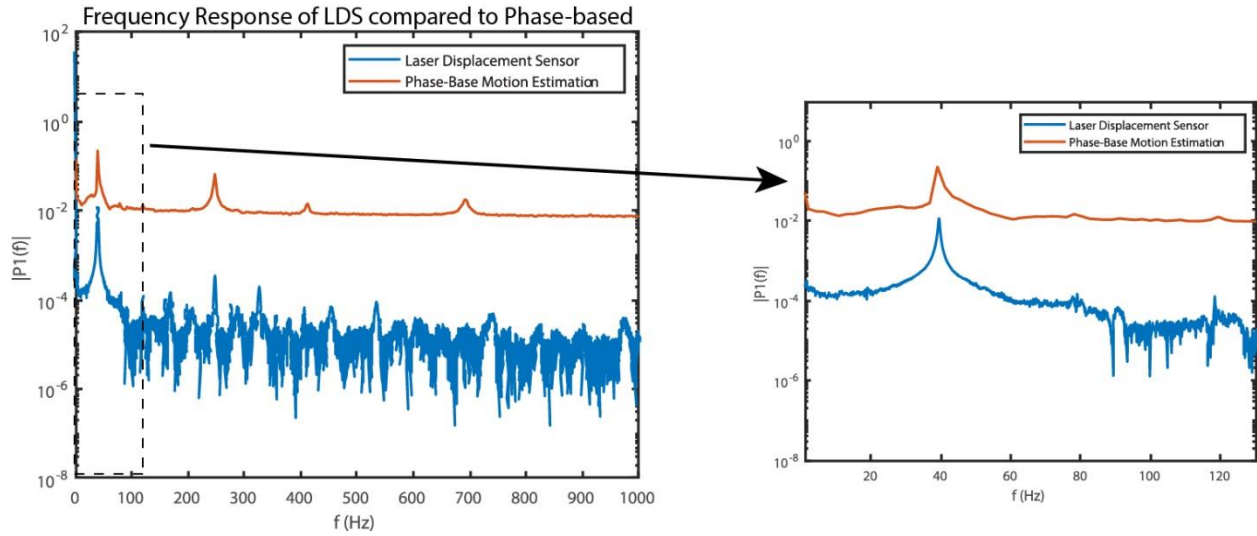


Figure 22: Frequency Response of Baseline PLA using LDS in Comparison with the Phase-based

The error obtained from the first, second and fourth mode shapes was 1.16 %, 0.04 %, and 0.06 %, respectively. This indicates that the phase-based motion estimation results are in great quantitative agreement with those of the LDS method. However, there was a slight increase of the error in the third mode shape (1.69 %), which may be attributed to the mode being normal to the camera's image plane making it challenging to detect (Figure 22).

Further validation was performed using the computer-generated simulation in ANSYS workbench. The results obtained from the simulation were compared with those from the phase-based motion estimation and LDS (Figure 23). The resonant frequencies obtained from the ANSYS simulation show an error less than 0.36 Hz for the first, second and fourth mode shapes when compared with the phase-based motion estimation. The third mode shape has a larger error due to out of plane motion.

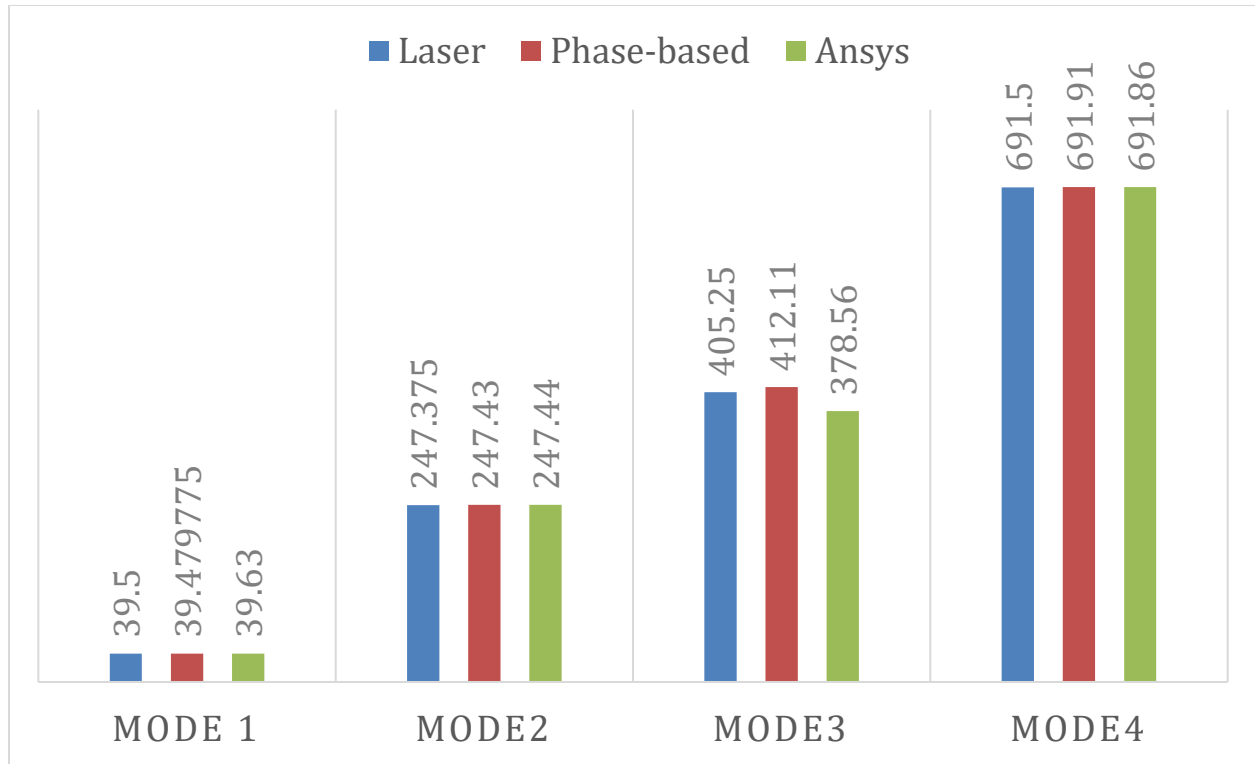


Figure 23: Resonant Frequencies of Baseline of PLA using ANSYS, LDS and Phase-based Motion Estimation

The results obtained from the ANSYS shows an average of 97.8% accuracy when compared with phase-based and 98.3% accuracy when compared with the LDS results. These validation processes clearly confirm the accuracy of resonant frequency extraction using the phase-based motion. This establishes a baseline signature in which subsequent parts were compared using phase-based motion estimation.

Damage Identifications

To analyze the phase-based motion estimation capability to detect defects in the PLA, 5 test specimens were initially designed and printed with increasing depths of the defect (0.1 mm, 0.5 mm, 0.7 mm, 1 mm, and 1.5 mm). This was done to ascertain the impact of varying defects on the natural frequency and mode shapes. Then, the same defect of 1.5 mm depth was introduced at

different locations on the beam (60 mm, 90 mm, and 120 mm from the base) to determine its effectiveness in determining defects at different locations.

Measurement of Severity of Defect

An intentional defect was introduced on the CAD model to produce a 25 mm by 0.2 mm defect near the fixed end of the beam as depicted in Figure 24. The parts were printed with the same dimensions as the healthy beams, but with varying depths of defects.

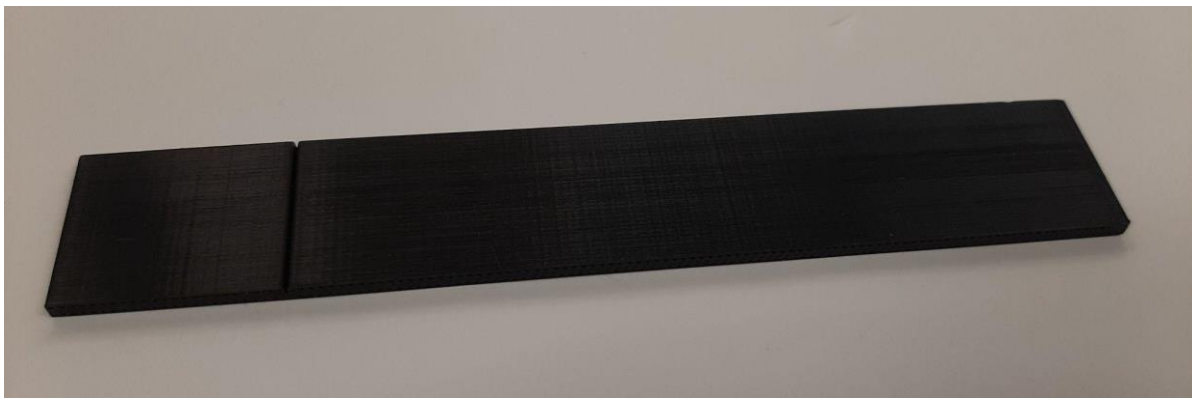


Figure 24: 3D Printed Test Model of a PLA Depicting the Defect in the Beam

Stage 1: First stage of defect, with the depth of void just over 3% (void depth of 0.1 mm) of the total thickness of the beam.

Stage 2: Second stage of defect, this has a void of just over 16% (void depth of 0.5 mm)

Stage 3: Third stage of defect, the depth of void was increased to just over 23% of the total beam thickness (void depth of 0.7 mm)

Stage 4: Fourth stage of defect, the depth of void was increased to just over 33% of the total beam thickness (void depth of 1 mm)

Stage 5: Fifth stage of defect, the depth of void was increased to 50 % of the total beam thickness (void depth of 1.5 mm). This defect was located at 30 mm from the fixed end of the beam.

Table 5: Frequency Comparison of a Healthy Baseline with Different Severity of Defect

Severity	Mode 1 (Hz)	Mode 2 (Hz)	Mode 3 (Hz)	Mode 4 (Hz)
Healthy (Baseline)	39.04	247.27	412.11	691.91
0.1mm	38.66	244.83	410.2	682.95
0.5mm	38.31	244.24	411.85	682.43
0.7mm	38.12	243.98	411.72	686.19
1mm	36.66	244.4	407.33	688.00
1.5mm	36.22	243.98	404.09	688.1

Figure 25 provides a visual representation of the frequency response of the baseline in comparison with the five defective materials. Having established the baseline response from the validation process, this phase-based motion estimation technique is also applied to the damaged PLA.

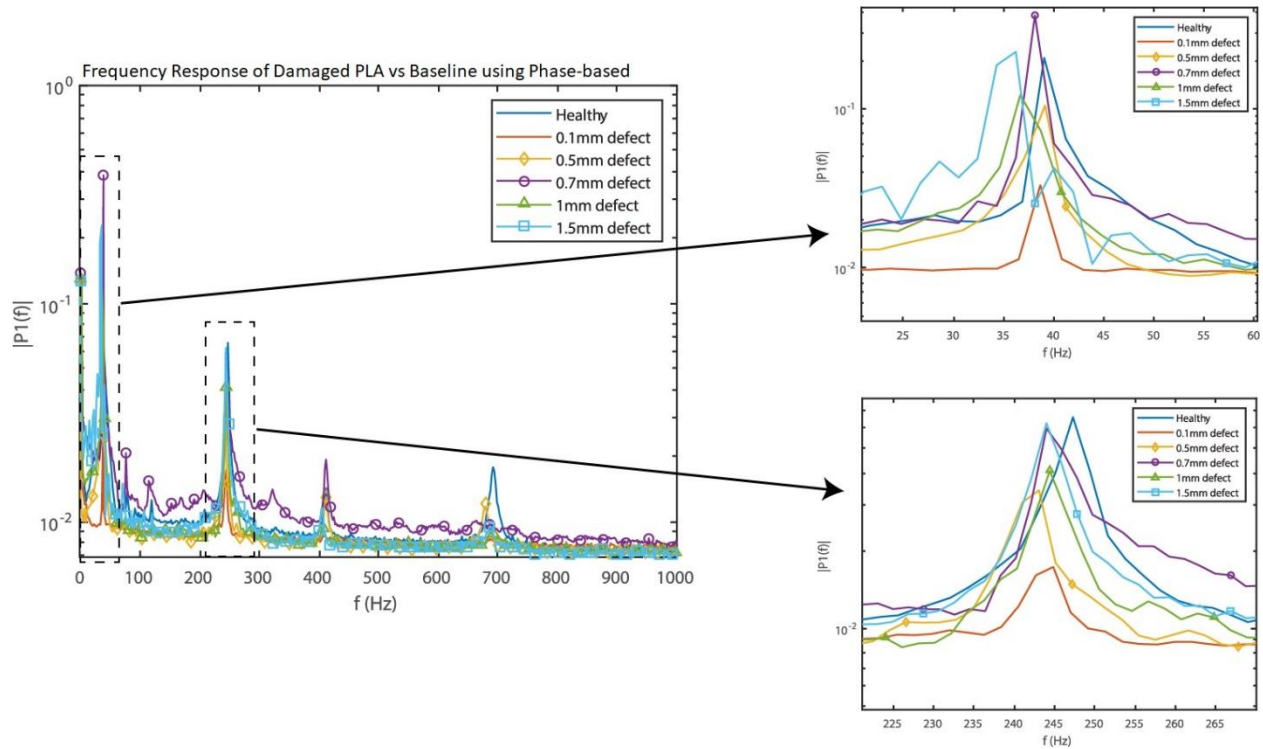


Figure 25: Frequency Response Representation of Phase-based Motion Estimation of Healthy and Varying Degree of Defect of PLA

As observed from Figure 25, the 0.1 mm depth defect value closely matches that of the baseline when the first mode shape is taken into consideration. This value decreases as the damage depth begins to increase from 0.1 mm to 1.5 mm (Figure 26). There is a sharp drop in value between the baseline and the 0.1 mm damage depth when the second mode shape is taken into consideration, but decreases gradually as the defect reaches 0.7 mm and then increases at 1 mm before decreasing again at 1.5 mm. It is assumed that the parts are free from any other form of defects apart from that which was intentionally introduced.

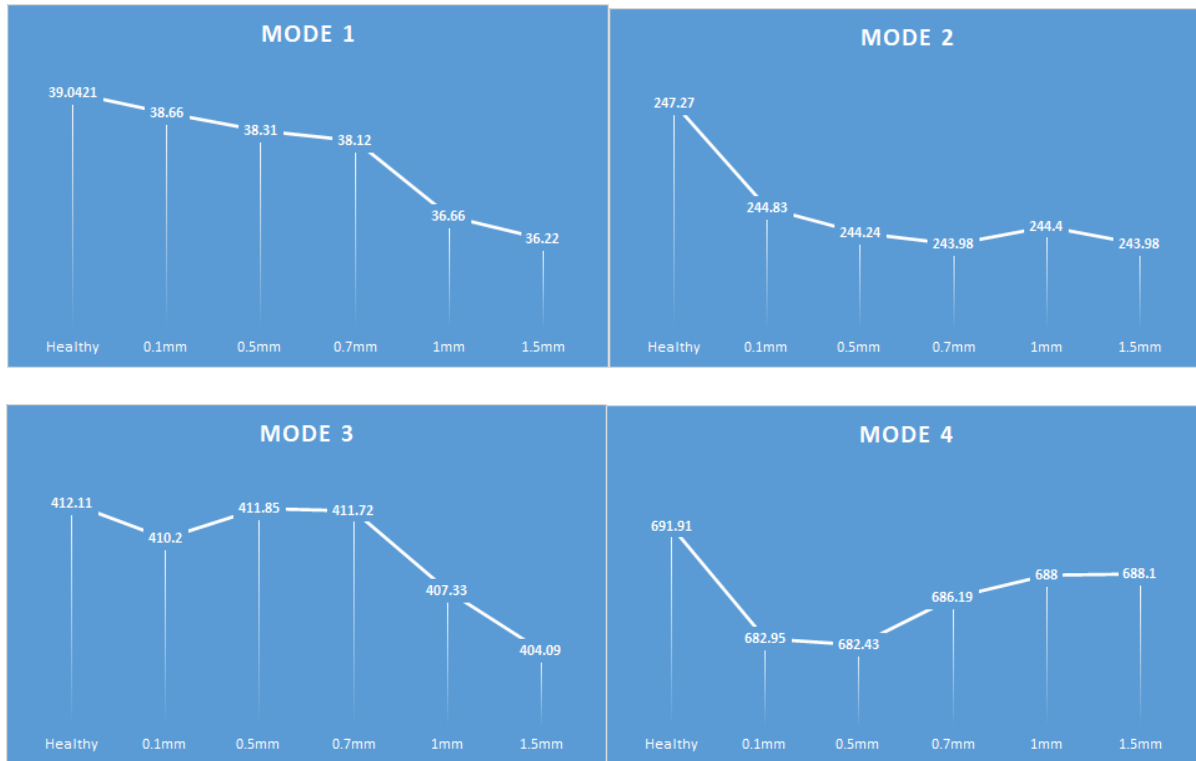


Figure 26: Graphical Representation of Different Frequency Modes of PME for Healthy and Different Degree of Defect

Measurement of Varying Void Location

Three more beams were fabricated with a void depth of 50% (1.5 mm depth) of the total beam thickness located in three different locations in the beam.

Stage 1: void located at over 30 % of the total length of beam (60 mm from one end).

Stage 2: void located at over 50 % of the total length of beam (90 mm from one end).

Stage 3: void located at over 70 % of the total length of beam (120 mm from one end).

This simulates defects in different locations on the desired parts.

Table 6: Frequency Comparison of a Healthy Baseline with Defect at Different Locations

	Mode 1 (Hz)	Mode 2 (Hz)	Mode 3 (Hz)	Mode 4 (Hz)
Healthy	39.0421	247.27	412.11	691.91
120 mm	38.51	236.2	408.22	629.01
90 mm	37.87	216.91	406.28	654.17
60 mm	36.16	229.04	407.85	642.92

The results obtained from the phase-based motion estimation technique in detecting the same damage at different locations are summarized in Table 6. For the first mode, the frequency shift is minimal when the damage is near the tip (120 mm), while the frequency is at maximum when the damage is located near the fixed edge (60 mm). The second order mode has the largest frequency shift when the damage is located near the center of the beam (90 mm), a similar situation is also observed in the third mode shape (Figure 27)

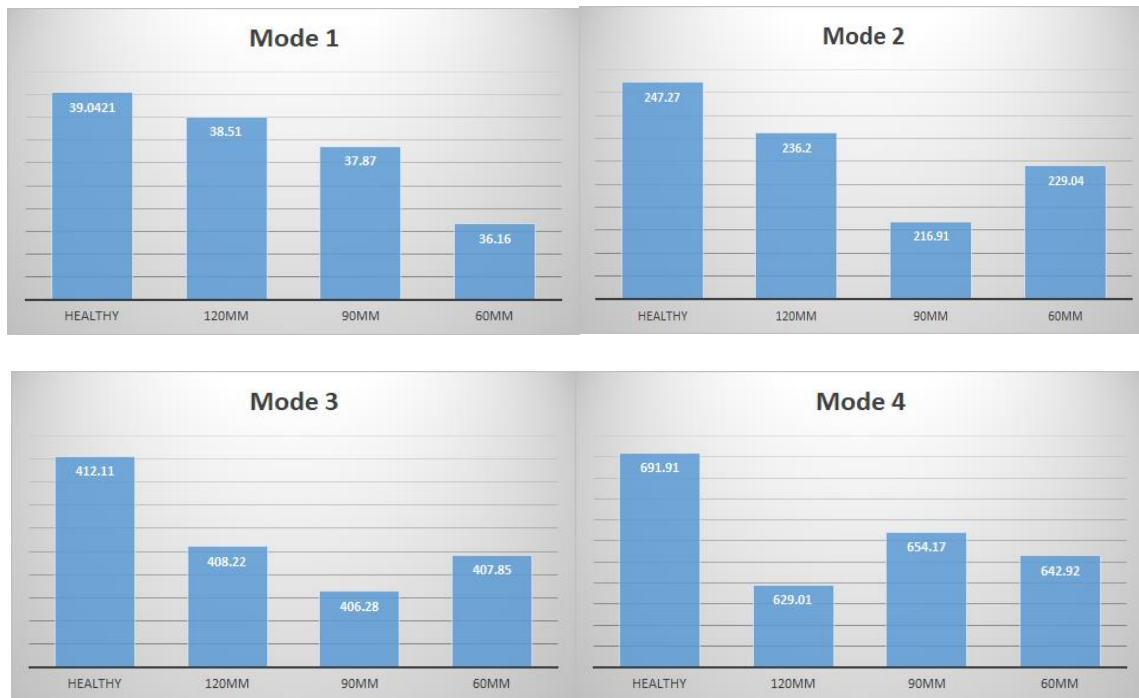


Figure 27: Graphical Representation of Different Frequency Modes of Healthy and Defective beam at Different Location using Phase-based Motion Estimation

These results suggest that certain mode shapes may be suitable for detecting the defects in the material. For example, the first mode shape shows a uniform increase in resonant frequency starting from the fixed point to the tip of the beam. Other mode shapes respond to the change in location of the defect in accordance with the deflection of the operating mode shapes, which can be seen when these mode shapes are isolated using the motion magnification algorithm.

Motion Magnification

The magnification was performed using a phase shifting Gabor filter. A Gaussian pyramid was applied with the magnification factor α that is carefully selected for each bandpass-filtering. The magnification factor α indicates the magnitude of the amplification, which enables the extraction of motion. The cutoff frequencies ω_l (low cutoff) and ω_h (high cutoff) indicate the frequencies utilized for bandpass- filtering, and f_s is the frame rate obtained from the high-speed camera (3270.86 Hz). This process can be used to amplify non-periodic motions by tuning to the frequency of the temporal bandpass filter and adjusting the low cut-off and high cut-off frequencies accordingly. As observed from Table 7, higher magnification factor (α) was selected for higher order mode shapes because higher order modes have less displacement contribution to the overall magnitude of the motion (Sarraf et al. 2018). The width of the bandpass filter selected for the first mode is 3 Hz, 5 Hz for the second mode, 10Hz for the third mode, and 20 Hz for the fourth mode. The choice of this narrow bandpass filter ensures that the right motions within the frequency range are amplified.

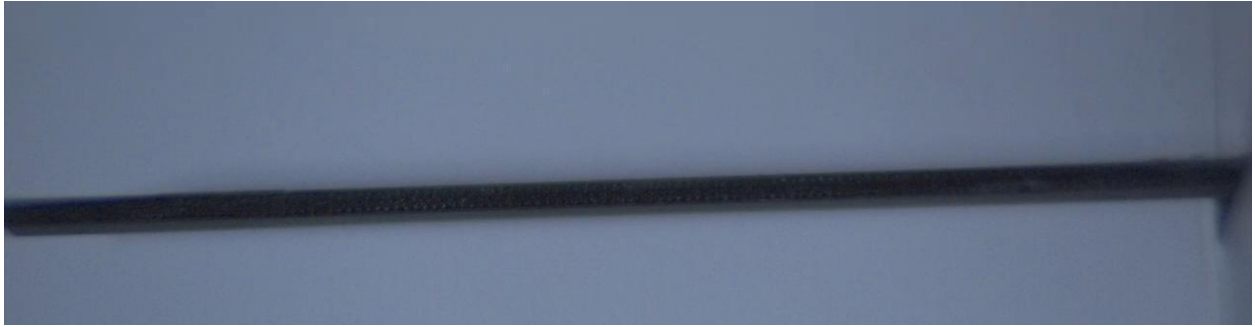


Figure 28: Original Image of the PLA



Figure 29: Second Mode Shape magnification of the PLA

Table 7: Motion Magnification Input Parameters

Video	Magnification factor (α)	Low cutoff frequency (ω_l (Hz))	High cutoff frequency (ω_h (Hz))
First Mode	20	36	42
Second Mode	100	242	252
Third Mode	200	402	422
Fourth Mode	200	671	711



Figure 30: Frame before Magnification

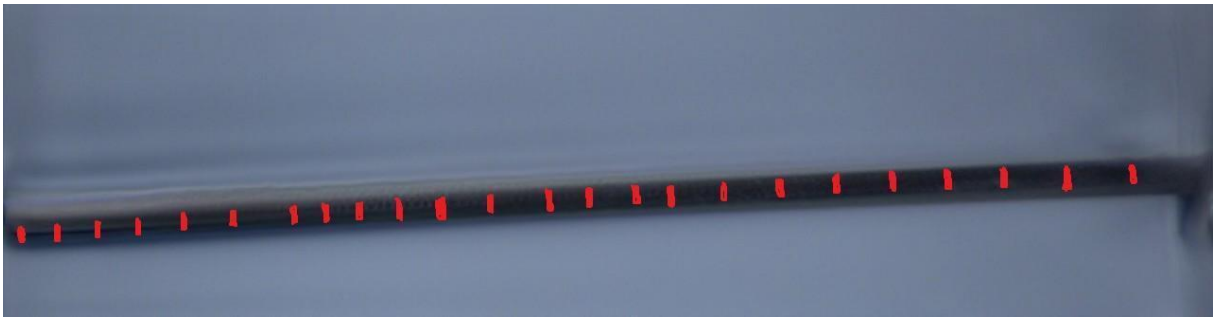


Figure 31: First Mode Shape

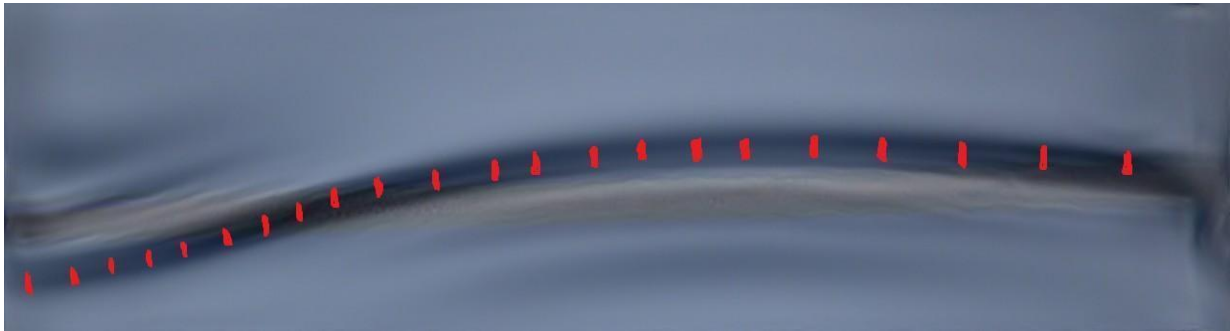


Figure 32: Second Mode Shape

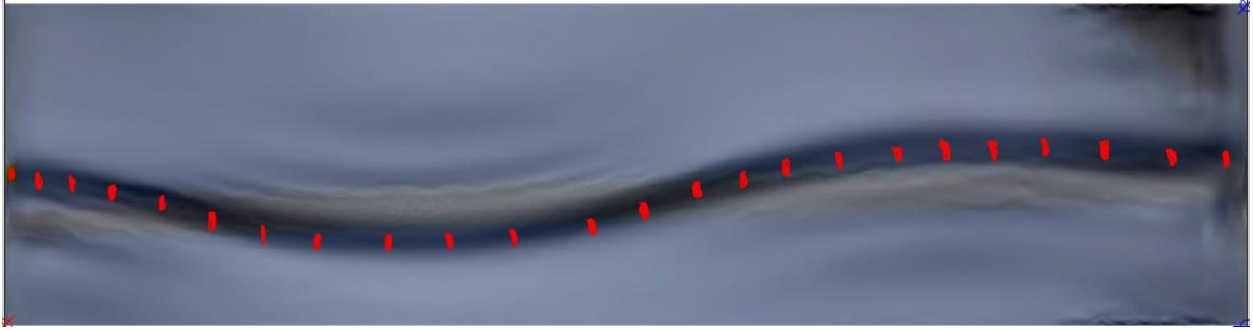


Figure 33: Third mode shape

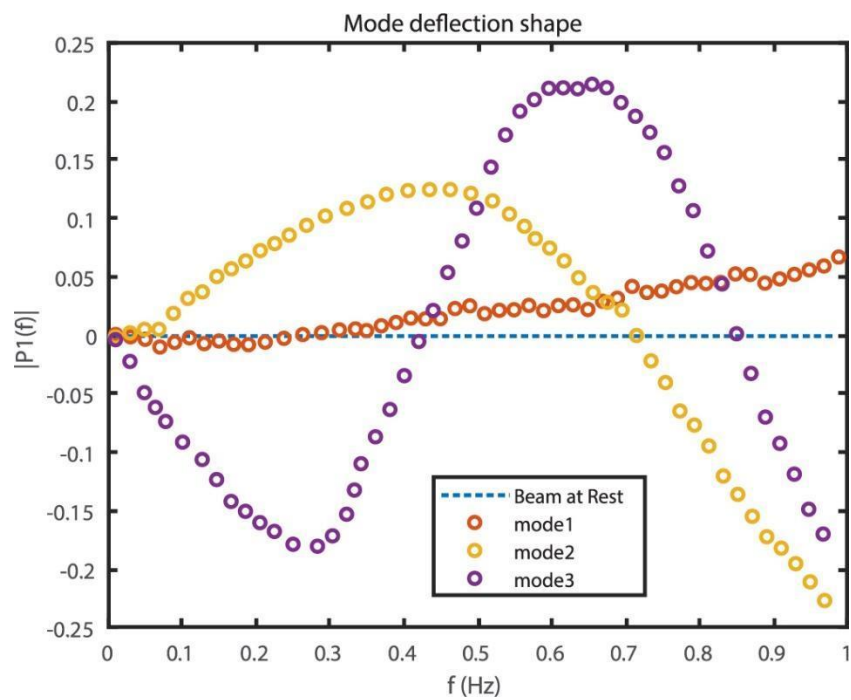


Figure 34: Graphical Representation of Operational Mode shapes of Phase-based method for Healthy Beam

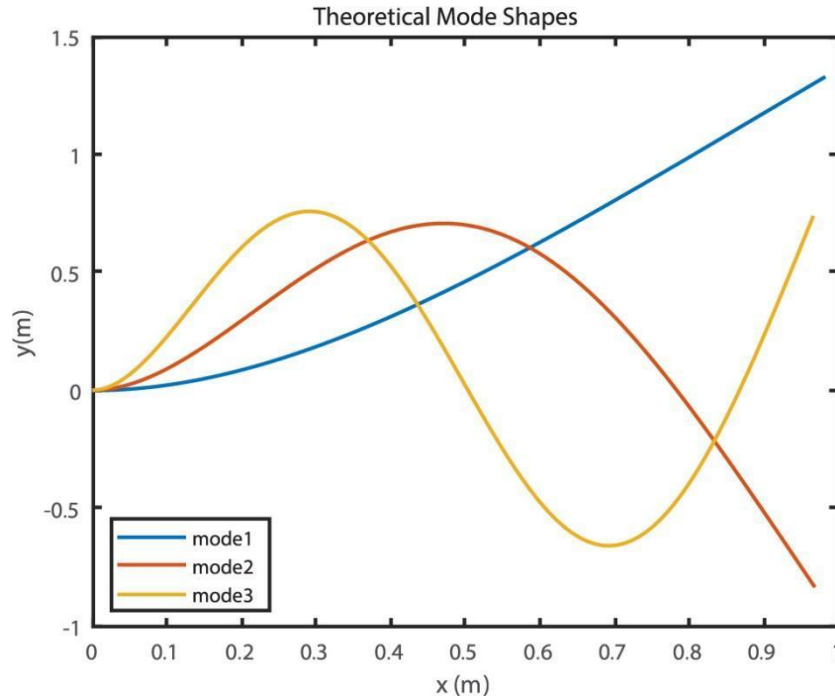


Figure 35: Theoretical Mode Shapes

The amplified motion may be considered as the operational mode shape at the desired resonant frequency. After magnification, an edge detection algorithm was utilized to extract the coordinates of the pixels associated with the boundary of the PLA beam being investigated. For a more accurate result, the edge detection algorithm was used with a data point extraction algorithm from pixels. After applying these algorithms, pixel calibration was performed on the image in the horizontal and vertical axis on a range of 0 – 1 mm. Figure (34) shows the calibrated data from the experimentally extracted mode shapes. After pixel point locations were performed, the result obtained clearly indicates that the operational mode shapes using motion magnification and theoretical calculations agree (Figure 35).

Comparison of Experimental Result with the Simulation

Figure 36 shows the simulation results obtained by using the harmonic response tool in ANSYS to obtain the deflection mode shapes. The simulation results were found to be qualitatively matching to the motion magnification results with an error of resonance frequencies less than 0.5 Hz across all mode shapes, except for the third mode due to out-of-camera-plane motion (Table 8).

Table 8: Frequency Comparison of Healthy Baseline with Experimental Result

Mode Shapes (Hz)	ANSYS	Phase-based method	Error
Mode 1	39.627	39.0421	0.5849
Mode 2	247.44	247.27	0.17
Mode3	378.56	412.11	33.55
Mode4	691.86	691.91	0.05

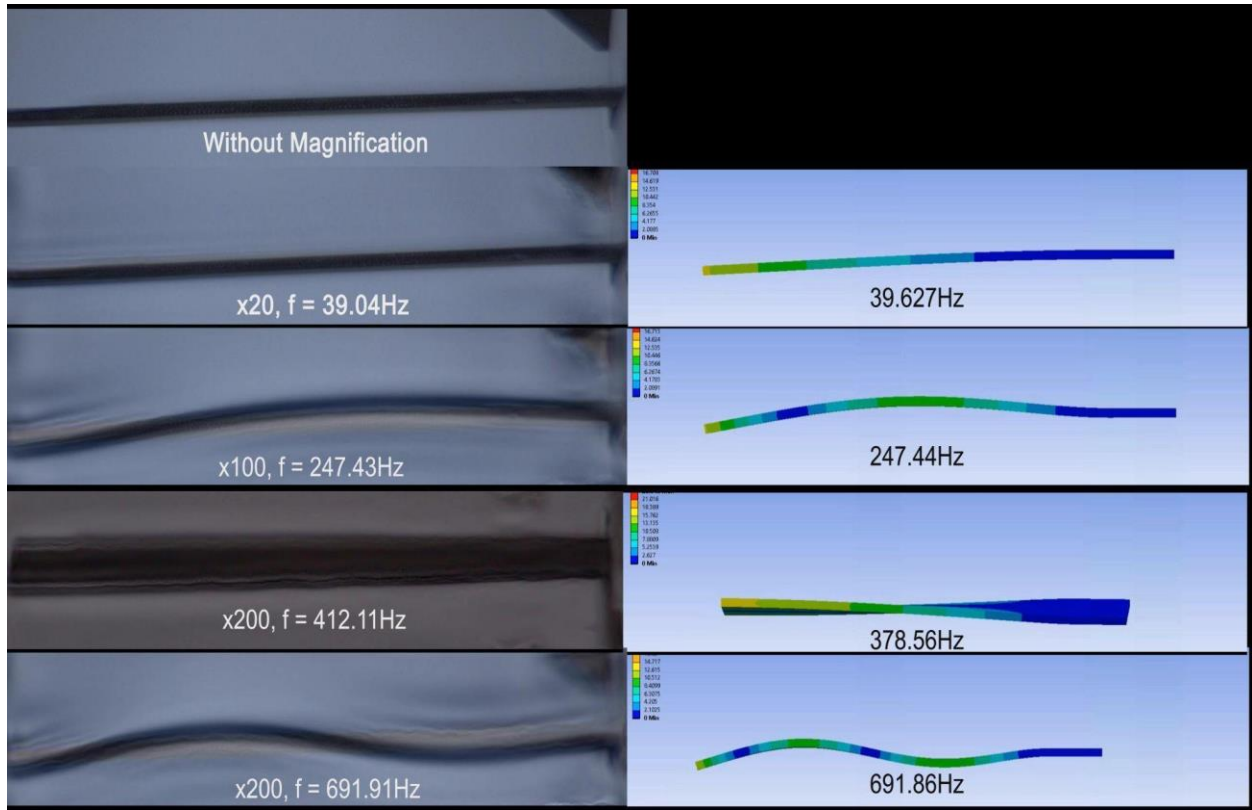


Figure 36: Numerical Simulation of the Operational mode shape of the PLA Compared with the Experimental Results

Modal Assurance Criterion (MAC)

To further validate the accuracy of the extracted mode shapes, the MAC values between the acquired mode shapes from the phase-based estimation and the theoretical mode shapes were calculated. Figure 37 shows a MAC value higher than 89% which is closer to unity. These results affirm the consistency of the modal vectors, thereby validating the results obtained using the motion magnification algorithm.

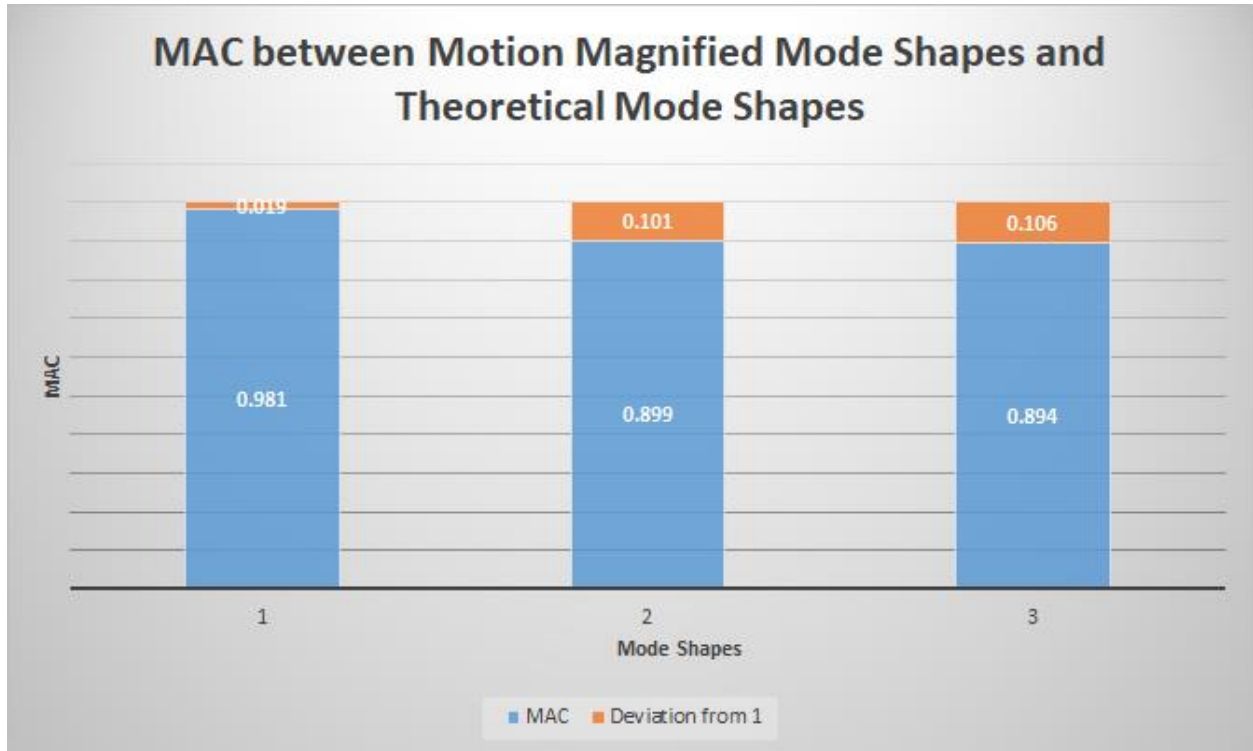


Figure 37: The MAC Estimation of the mode shapes using Phase-based Motion Magnification

To obtain the MAC value of the defective beams, the same process was performed for each defective PLA structure. The motion magnification algorithm was applied to amplify the motion with the appropriate bandpass frequency that corresponds to the resonant frequency of the defective PLA structure. The resulting videos produce each operational mode shape of the PLA structure. Figures 38 - 40 show two frames of each mode shapes at their maximum displacements. The mode shapes extracted by edge detection algorithms were applied to extract the MAC values. Each pair of the image frame is denoted with “+1” and “-1”, respectively corresponding to 0° and 180° phase changes.

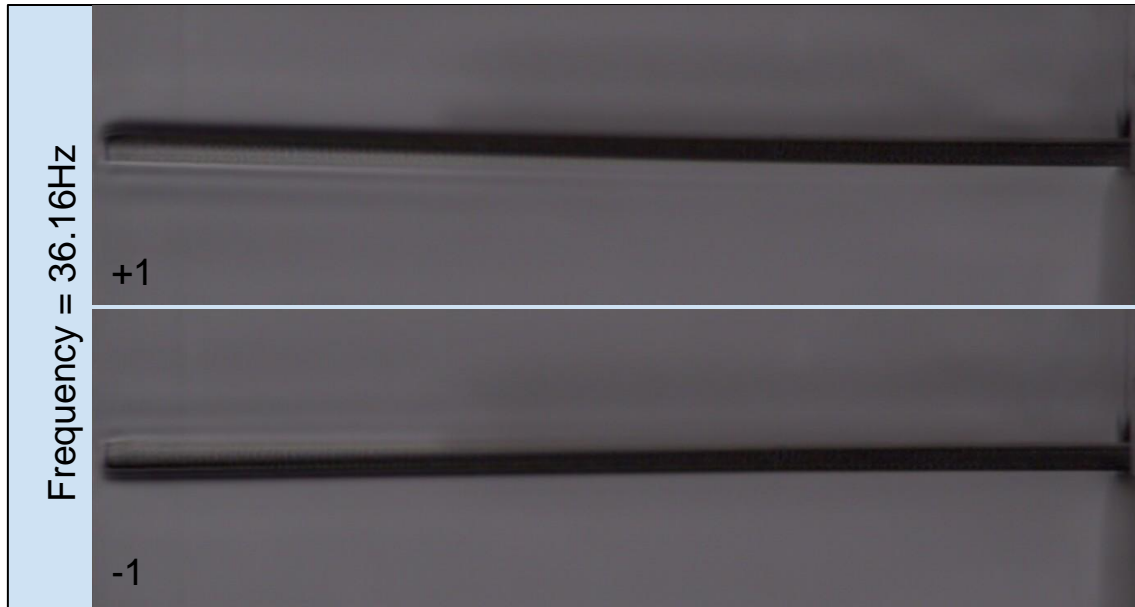


Figure 38: Frame at Maximum Displacement of the Defective PLA for the First Mode frequency of 36.16Hz and Magnification Factor of 20

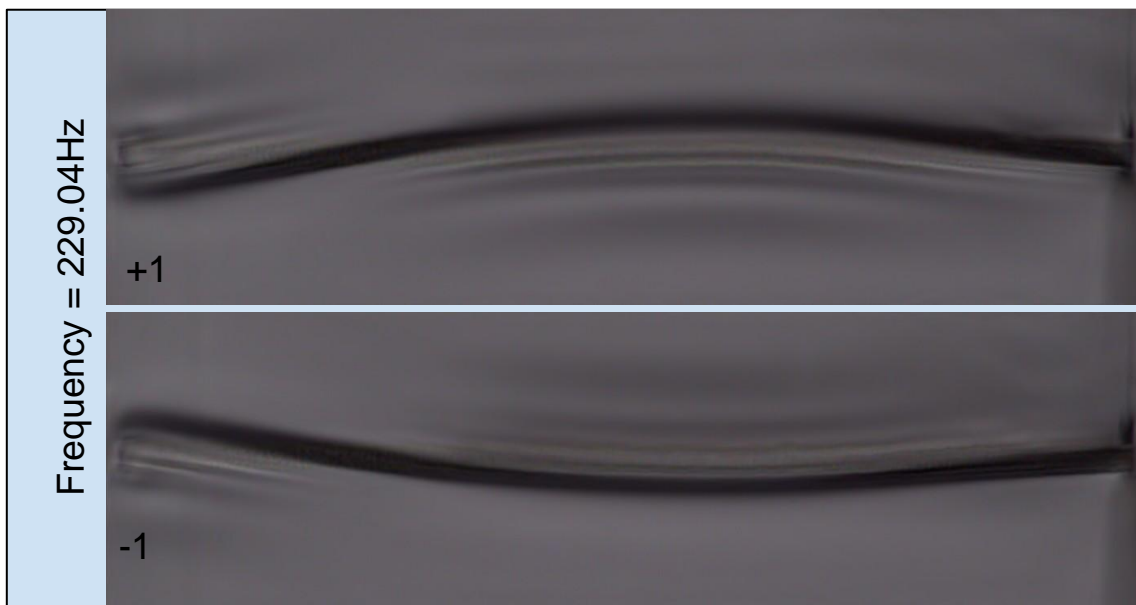


Figure 39: Frame at Maximum Displacement of the Defective PLA for the Second Mode frequency of 229.04Hz and Magnification Factor of 100

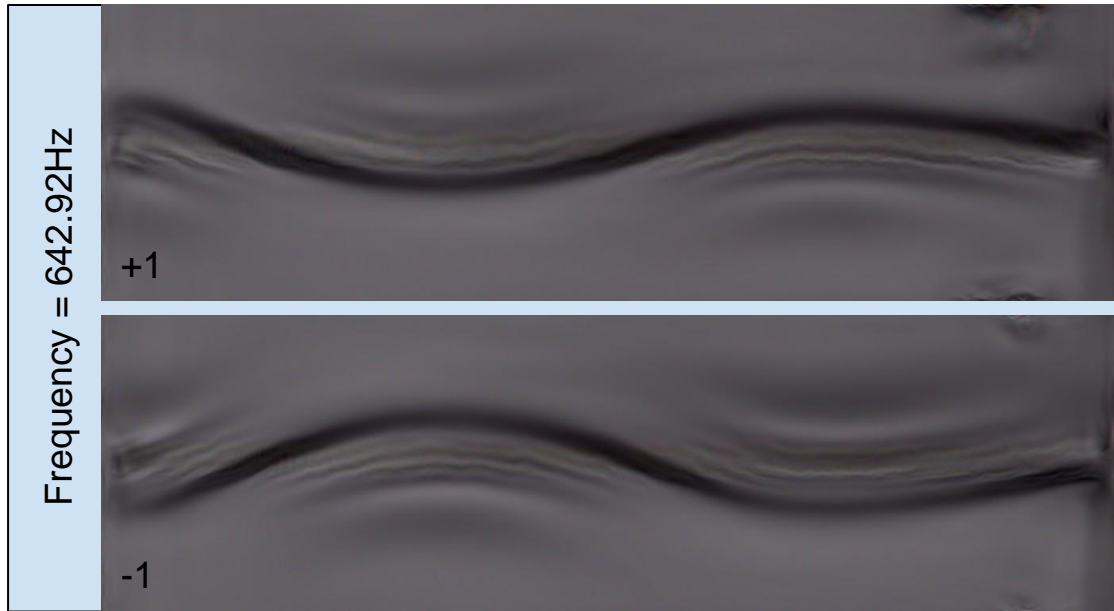


Figure 40: Frame at Maximum Displacement of the Defective PLA for the Second Mode frequency of 229.04Hz and Magnification Factor of 200

Figures 41 - 43 show the extracted operational deflection data for the healthy and the damaged PLA structures. A close observation of the first, second and fourth mode shapes show that there exists an obvious discrepancy in the mode shapes due to varying defects. For the first mode shapes, the maximum deflection of the PLA reduces as the defects are increased from 0 to 1 mm; however, at defect depth of 50% of the PLA thickness, the maximum deflection increases. The second mode shape shows a much higher deviation of maximum deflection for damage depth of about 15 % and 50 % of the total thickness of the PLA. On the other hand, for the damage of 30% depth, the deviation is indistinguishable from the baseline. The fourth operational mode shape also provides a clear difference in mode shapes due to the level of damages.

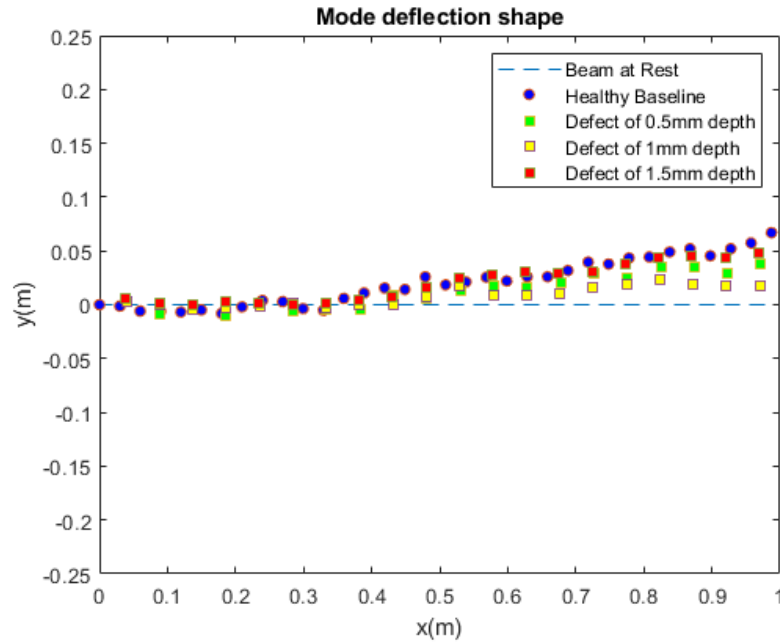


Figure 41: First Operational Mode Shape of Damaged PLA Compared with Healthy Baseline at its Maximum Deflection

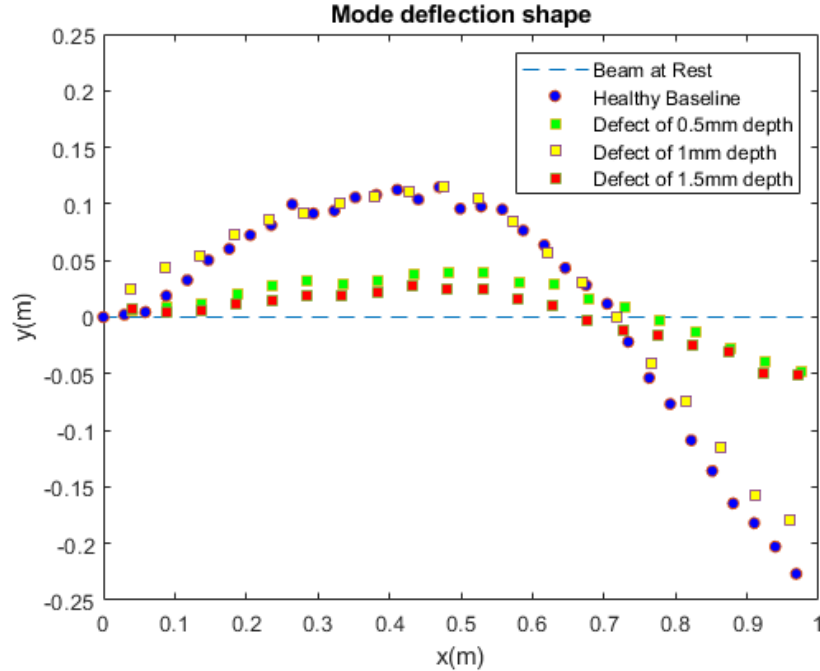


Figure 42: Second Mode Shape of Damaged PLA Compared with Healthy Baseline at its Maximum Deflection

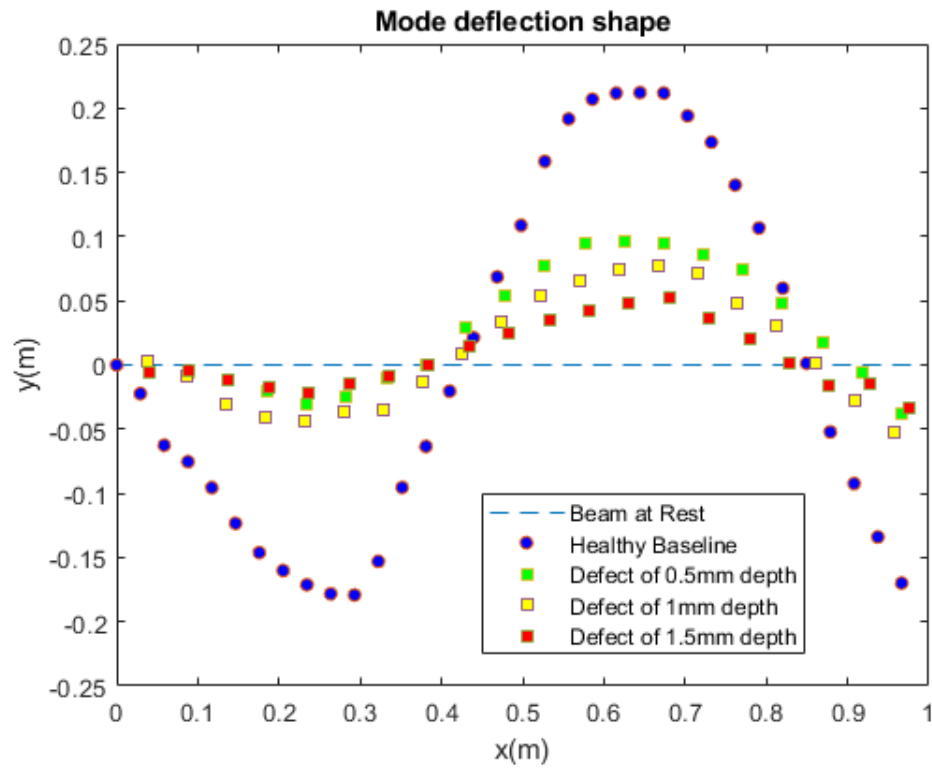


Figure 43: Fourth Mode Shape of Damaged PLA Compared with Healthy Baseline at its Maximum Deflection

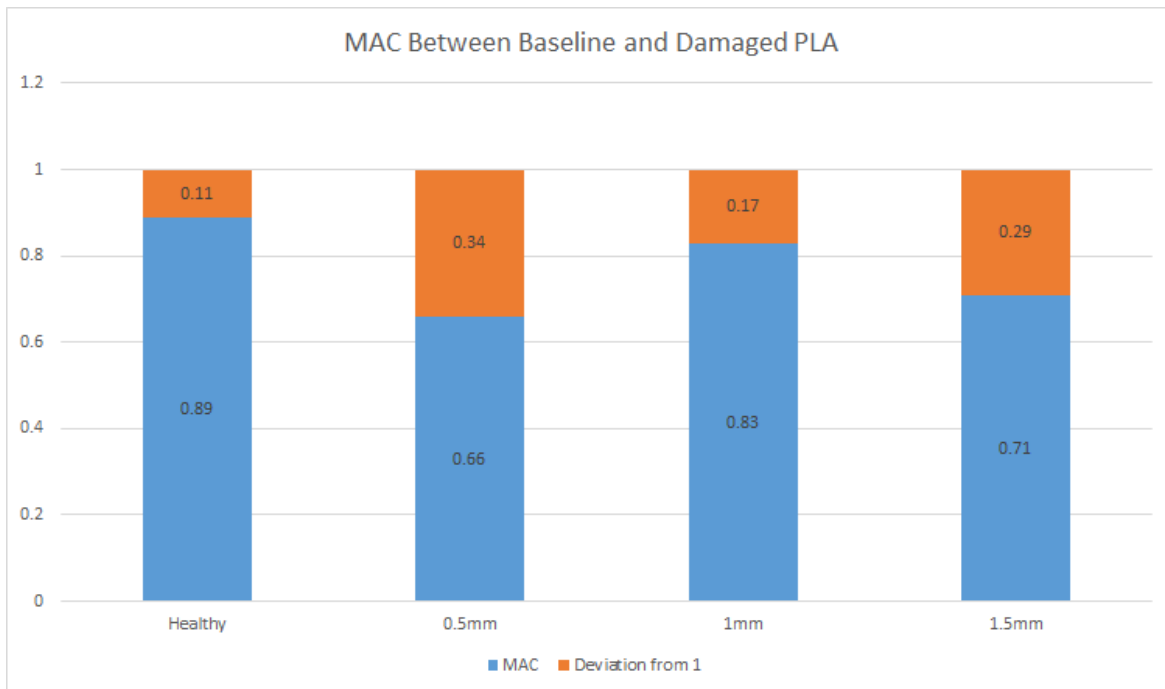


Figure 44: Estimated MAC Value of Operating Mode Shapes for Baseline and Damaged PLA

The MAC value was used to quantitatively compare the healthy PLA beam which serves as the baseline to various defective PLA beams. The magnitude of the operational mode shape considerably decreases for the fourth mode, which indicates the presence of damage in the beam (Figure 44). The MAC value of the 0.5mm depth defect was 66%, 83% for the 1mm defect and 71% for the 1.5mm, which were all lower than the baseline of 89%.

Figures 45-47 show the quantified operational mode shapes of the PLA beams when the damage occurs at different locations of the beam. The result was compared with the healthy baseline. The maximum deflection appears to be at the highest when the damage is located close to the tip of the beam; this is confirmed when the first and second operational mode shape is considered.

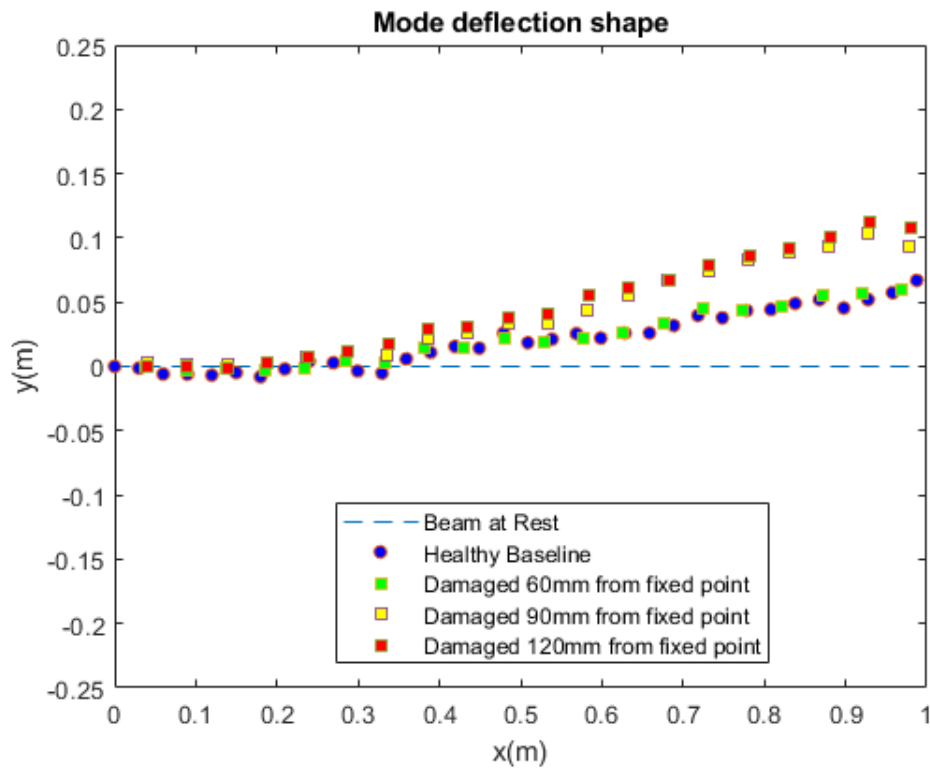


Figure 45: First Mode Shape of Damaged PLA at Different Location Compared with Healthy Baseline at its Maximum Deflection

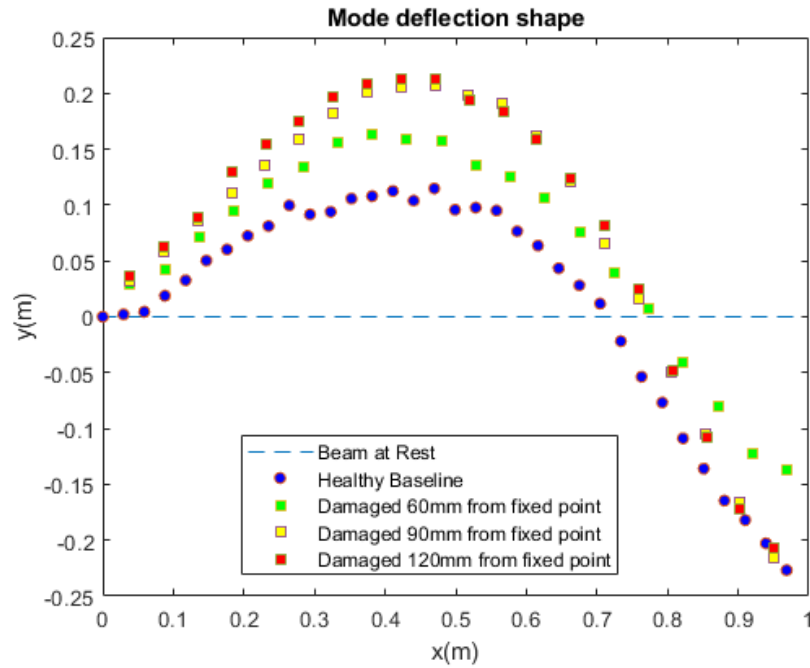


Figure 46: Second Mode Shape of Damaged PLA at Different Location Compared with Healthy Baseline at its Maximum Deflection

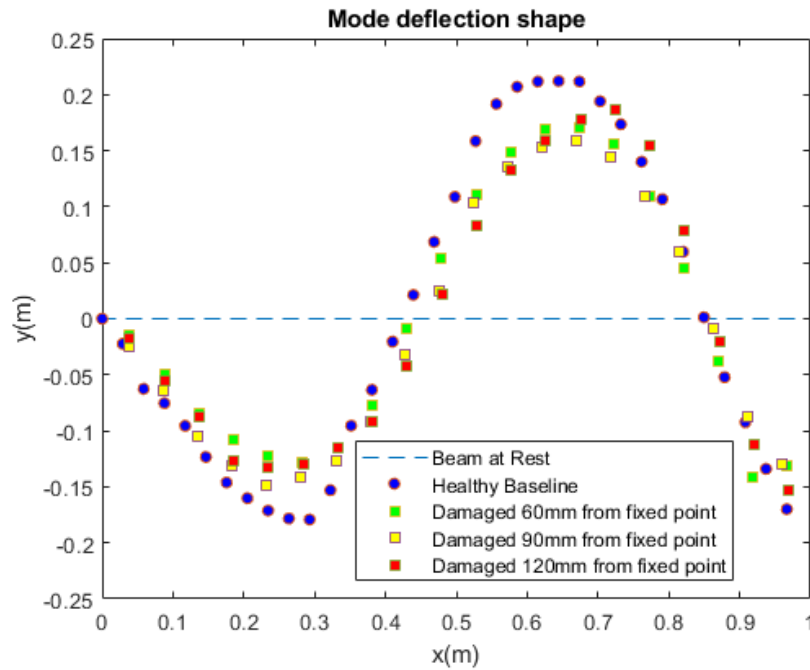


Figure 47: Fourth Mode Shape of Damaged PLA at Different Location Compared with Healthy Baseline at its Maximum Deflection

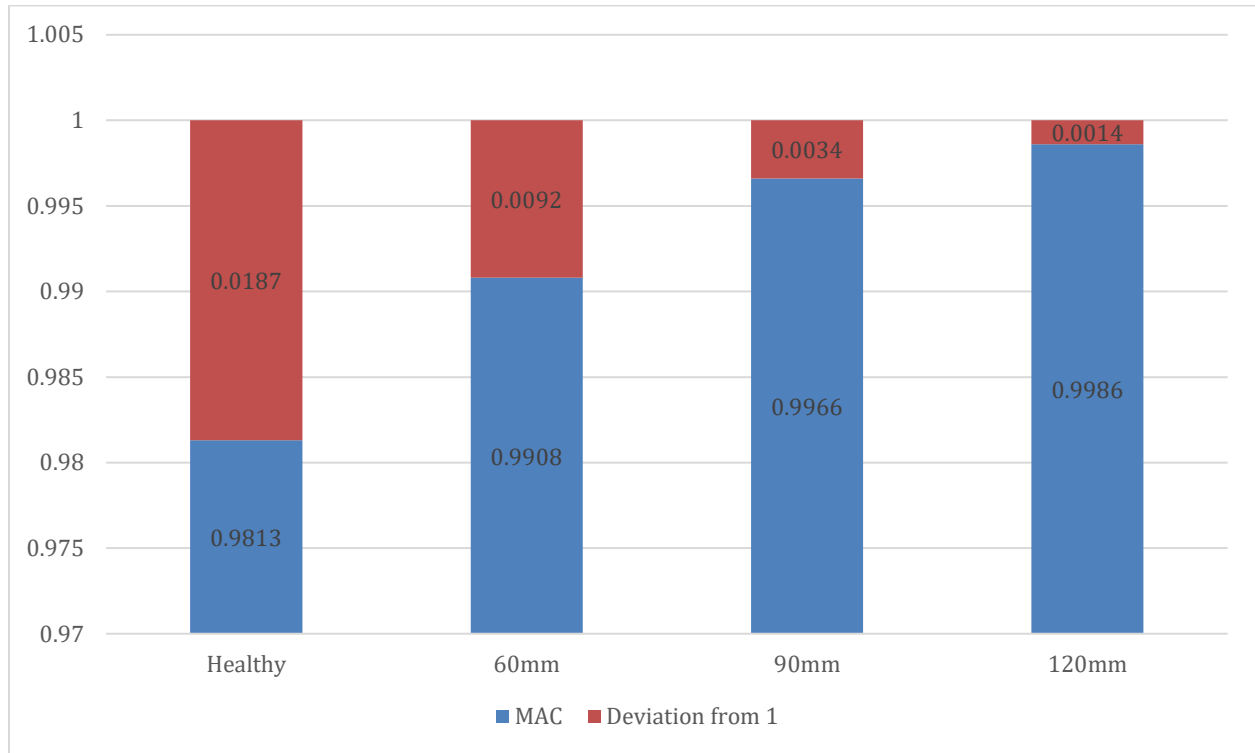


Figure 48: Estimated MAC Value of Operating Mode Shapes for Baseline and Damaged PLA at Different Location

Glass Fiber Reinforced Plastic (GFRP) Results

After the experimental and numerical validation of using the phase-based motion estimation method for identifying the damage characteristics of additive manufactured parts are conducted, this method was also utilized for analyzing samples of glass fiber reinforced plastic (GFRP) structures. This experiment involves the production of two GFRP: one serving as a baseline while an intentional defect was introduced to another sample. Table 9 summarizes the dimensions and mass of the two beams. The higher thickness value of the defective material was a result of an impurity. Figures 49 and 50 depict the two test samples of the GFRP used for the experiment.

Table 9: Dimension and Mass of GFRP

	Length(mm)	Width(mm)	Thickness(mm)	Mass(g)
Baseline Sample	151.87	25.40	2.68	16.49
Defective Sample	151.96	25.55	2.88	17.34

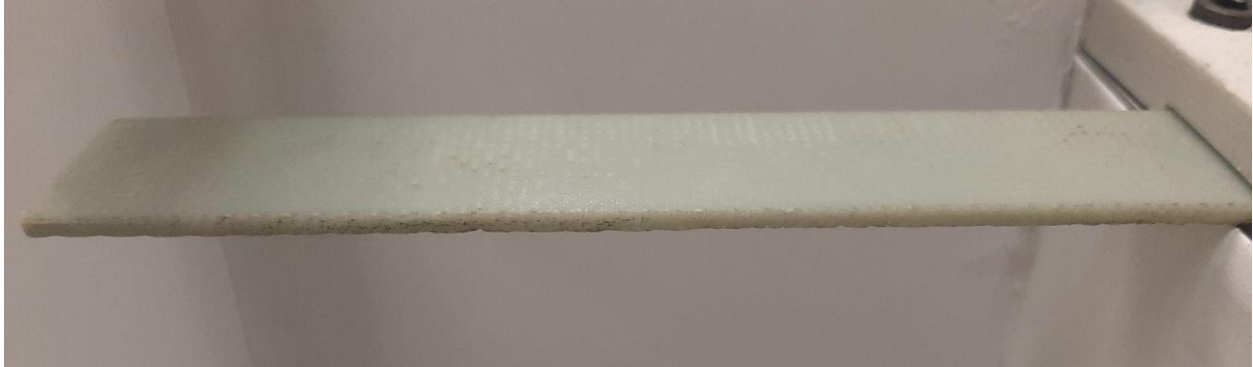


Figure 49: Image of the GFRP Baseline Material

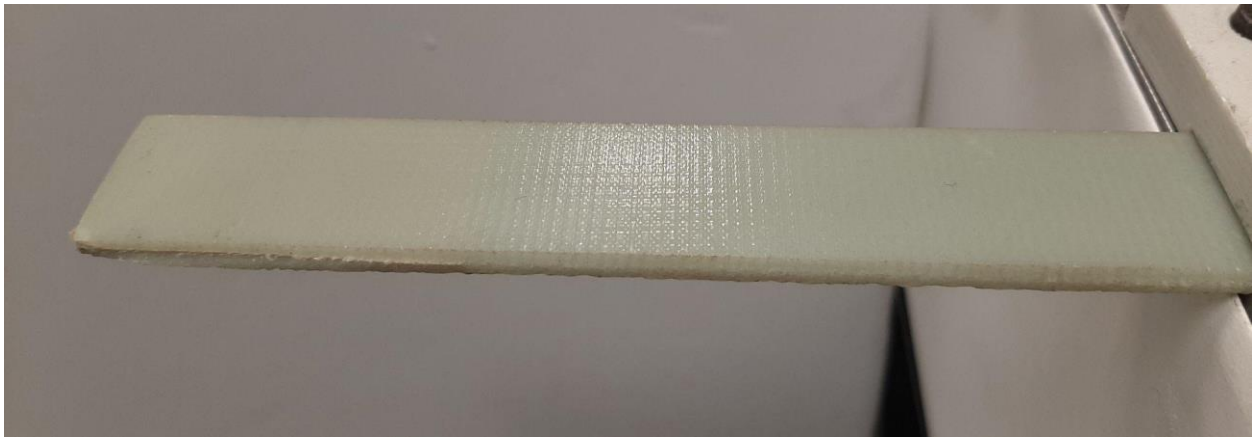


Figure 50: Image of the Defective GFRP Material

The natural frequencies obtained from this experiment are depicted in Figures 42 and 43. There was a shift in the first resonant frequency to the right when a defect was introduced to the pure material. However, there appears to be a frequency shift to the left when examining the second resonant frequency. The reduction in the resonant frequency continues for the third and fourth peak

frequencies when compared to that of the baseline, which implies stiffness reduction due to the damage.

Table 10: Frequency of Baseline and Defective Composite Material

	Mode 1 (Hz)	Mode 2 (Hz)	Mode 3 (Hz)	Mode 4 (Hz)
Baseline	60.30	376.42	539.05	1050.69
Damaged	66.45	352.93	462.2	953.94

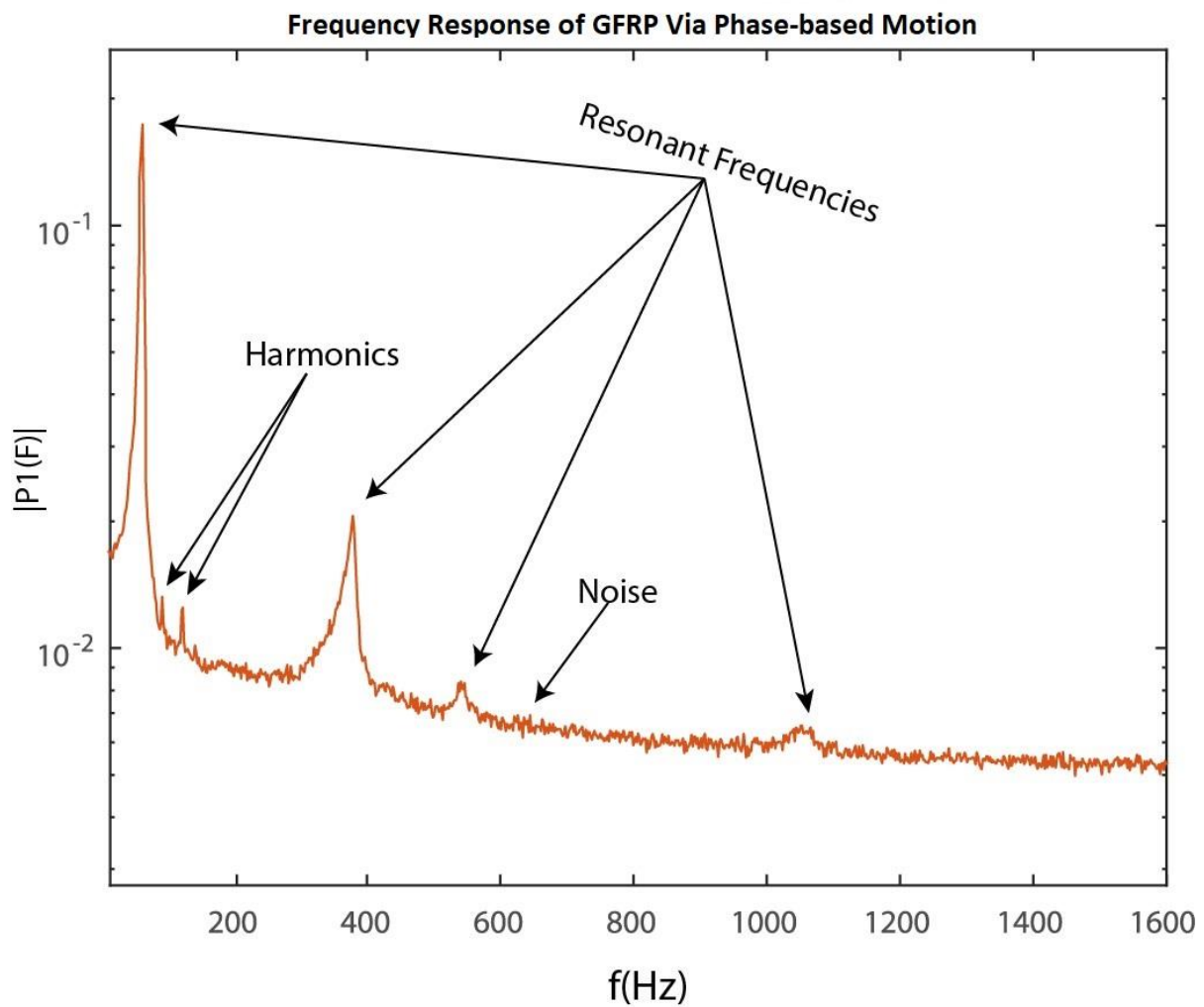


Figure 51: Frequency Response of Baseline GFRP

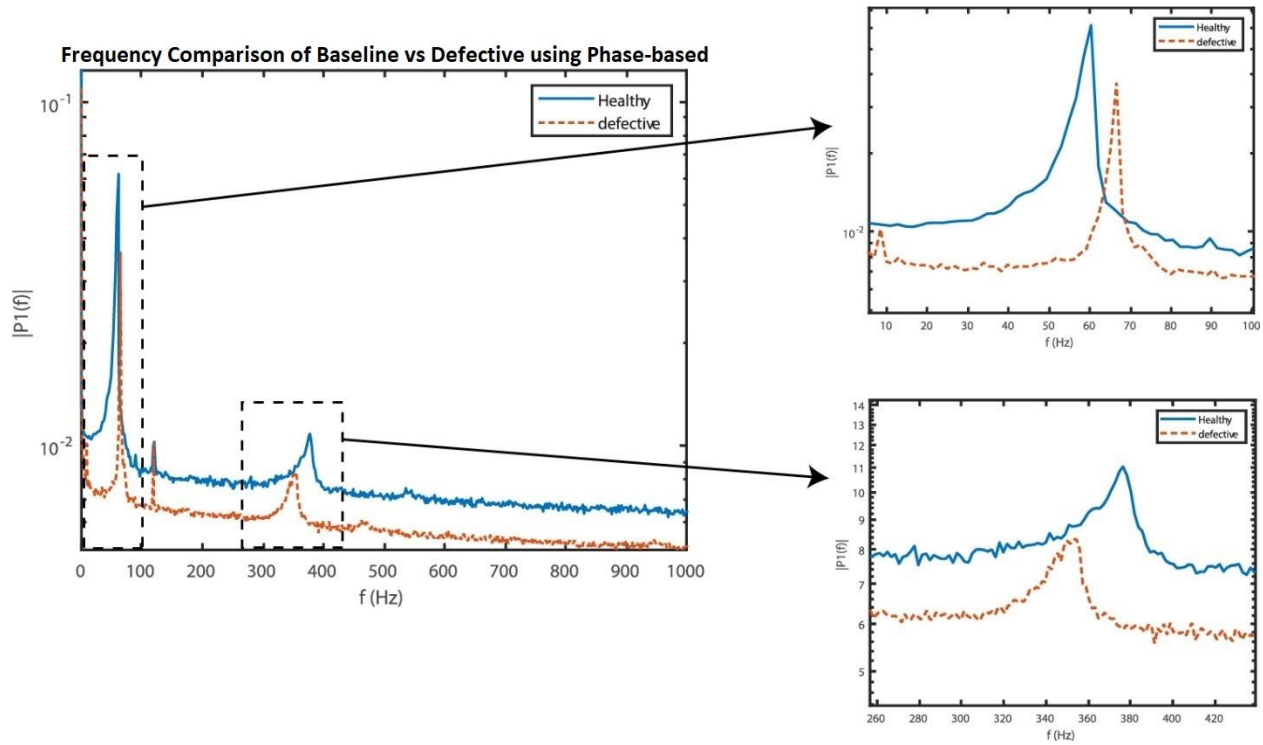


Figure 52: Frequency Response Comparison of Healthy and Defective GFRP using Phase-based motion Estimation

To extract the operational mode shape, the phase-based motion magnification algorithm was also applied to magnify the motion with an appropriate bandpass frequency that corresponds to the resonant frequencies of the structure. The original image of the GFRP before magnification is shown in Figure 53. The first operational mode shapes after magnification of 20 times its displacement is depicted in Figure 54. The second resonant frequency was magnified 200 times to extract its operational mode shapes.



Figure 53: Original Video Frame of GFRP without Magnification

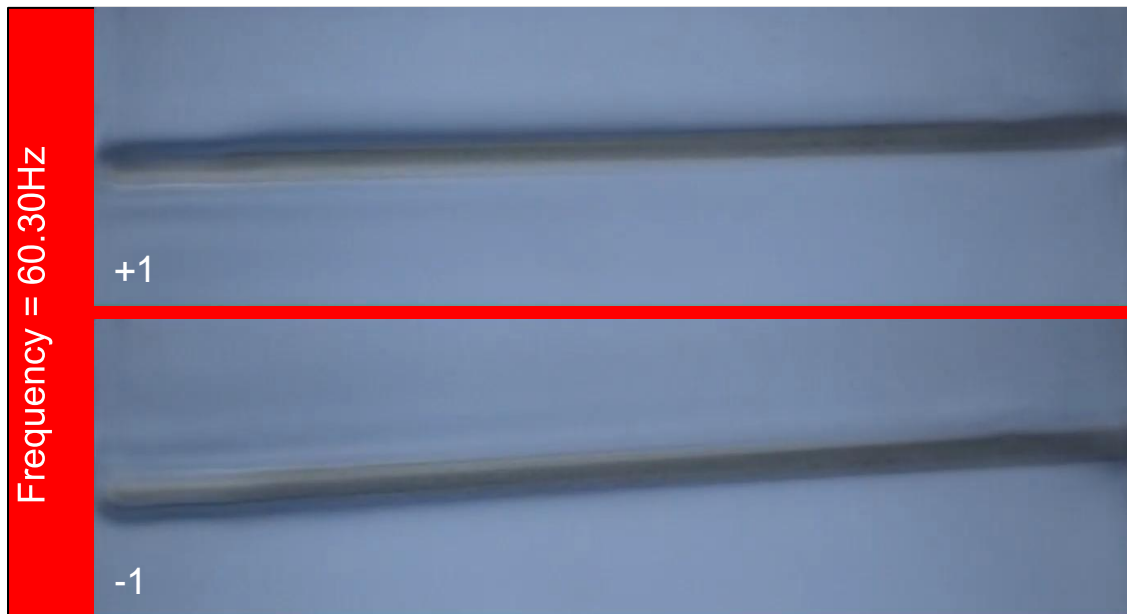


Figure 54: Image Frame at Maximum Displacement of the Magnified GFRP for the First Mode for Frequency of 60.30Hz, and Magnification Factor of 20

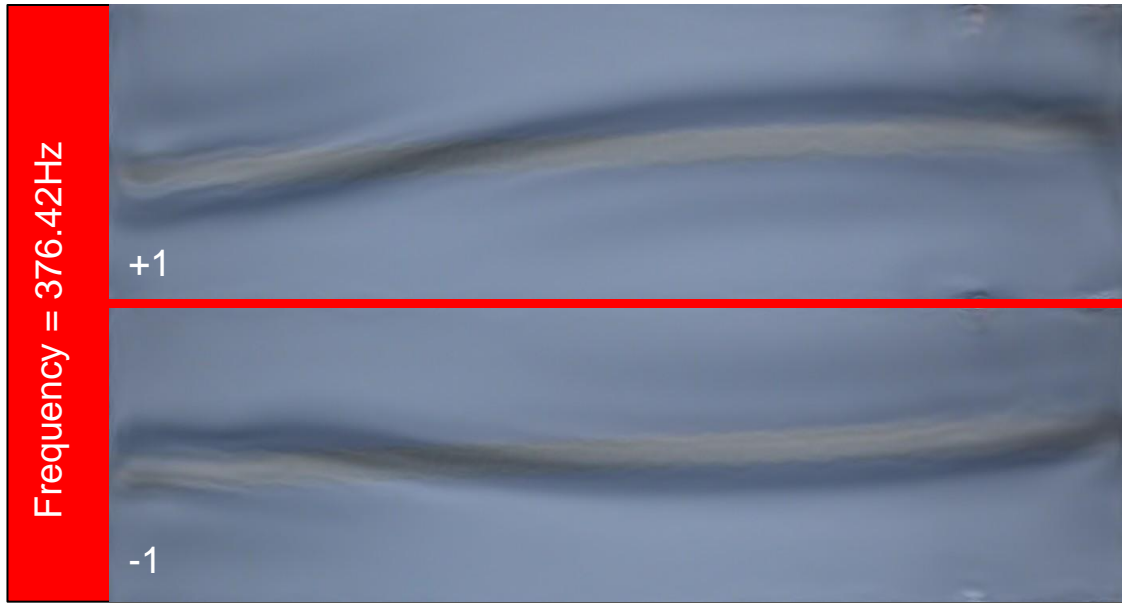


Figure 55: Image Frame at Maximum Displacement of the Magnified GFRP for the Second Mode Frequency of 376.42Hz, and Magnification Factor of 200

The magnification of this selected resonant frequency ensures that the motion at the desired frequency is predominant in the video. Extracting the quantitative vectors of operating deflection shape enable structural analysis.

Numerical Result of GFRP

The glass-fiber is an isotropic material and a commonly utilized filament. The most common types are E-Glass, C-Glass, S-Glass and AIR-Glass (Abbood et al. 2021). A finite element model was created using the ANSYS Workbench with the material properties shown in Table 11. The results obtained from the numerical analysis and experiment are presented in Table 12 and Figure 56. The maximum error between the resonant frequencies obtained by the phase-based method and those from the numerical analysis is less than 2.11%. Therefore, the two methods are in good correlation.

Table 11: Material Properties of GFRP used for Numerical Analysis

Material	Density (kg/m ³)	Modulus of Elasticity (GPa)	Poisson's ratio
E-glass GFRP	2500	14.6	0.22

Table 12: Frequency Comparison of Phase based with Numerical Analysis of GFRP Baseline

	Mode 1 (Hz)	Mode 2 (Hz)	Mode 3 (Hz)	Mode 4 (Hz)
Phase-based	60.30	376.42	539.05	1050.69
Numerical Analysis	60.22	376.58	550.68	1052.50
percentage error %	0.13	0.04	2.11	0.17

The operational mode shapes of the GFRP obtained by using the phase-based motion magnification algorithm were compared with those obtained by using numerical analysis in Figures 57 - 60. The obtained results clearly show that the two methods provide good quantitative agreement, which further validates the reliability of the phase-based motion magnification.

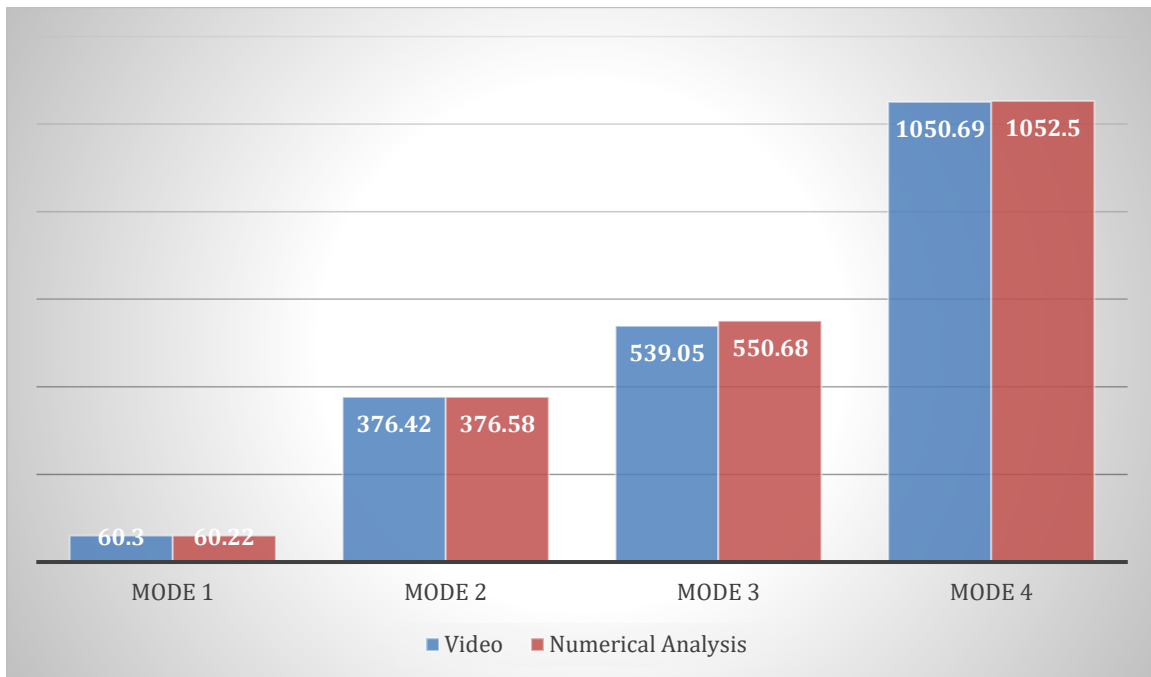


Figure 56: Frequency Comparison of Phase-based method and Numerical Analysis of GFRP

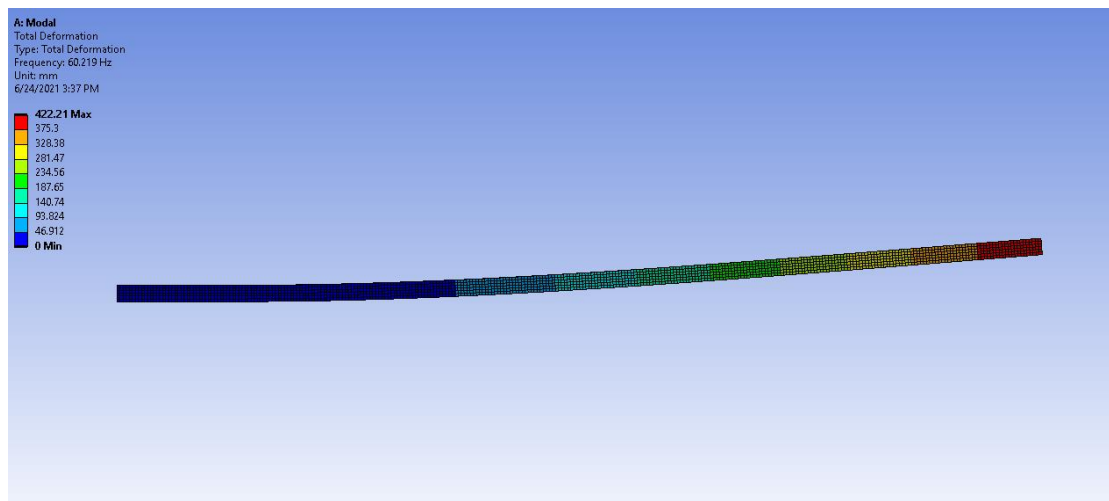


Figure 57: First Mode Frequency of GFRP

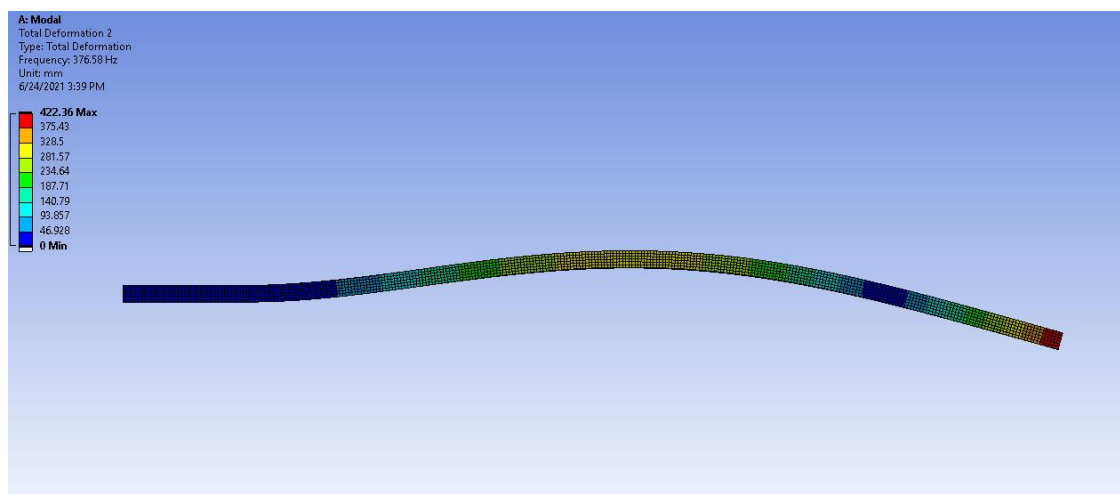


Figure 58: Second Mode Frequency of GFRP

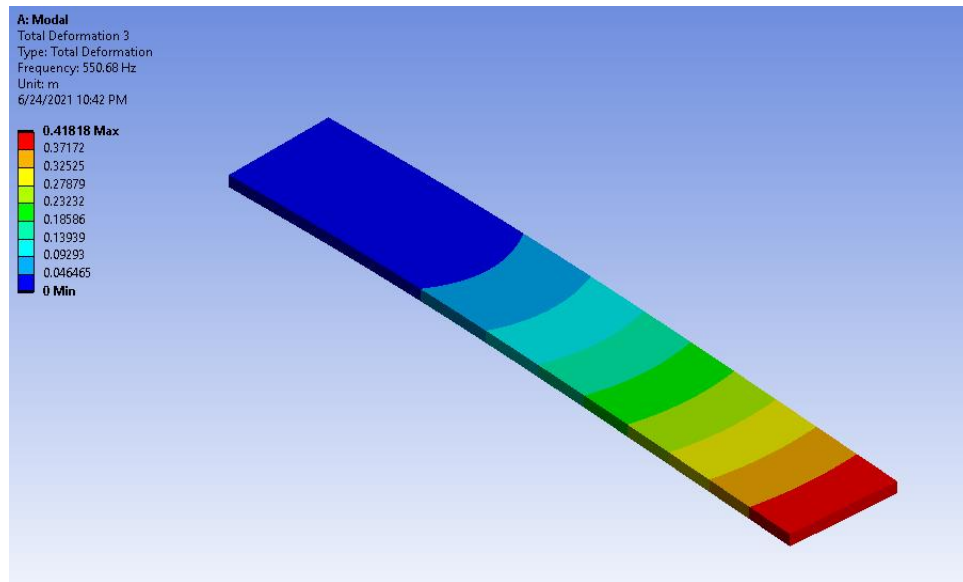


Figure 59: Third Mode Frequency of GFRP

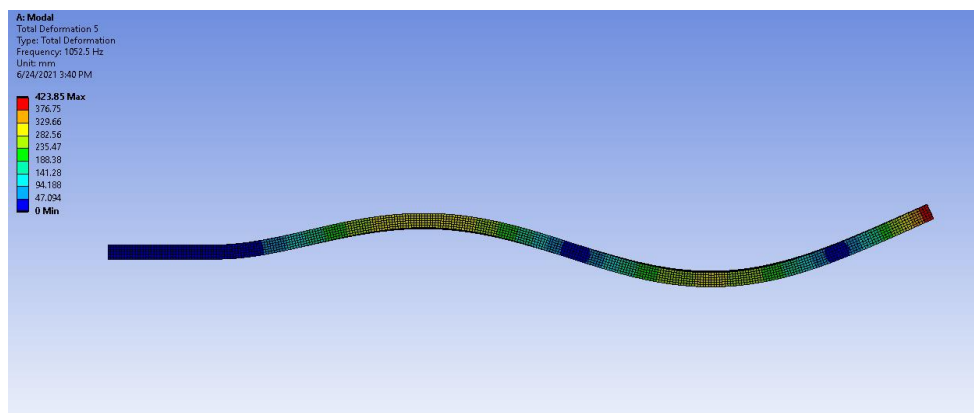


Figure 60: Fifth Mode Frequency of GFRP

This operational mode shape was further used to determine the presence of defects in the GFRP using the phase-based motion magnification algorithm. The results are depicted in Figures 61 and 62, where one can observe the discrepancy in the two mode shapes due to the presence of defects.

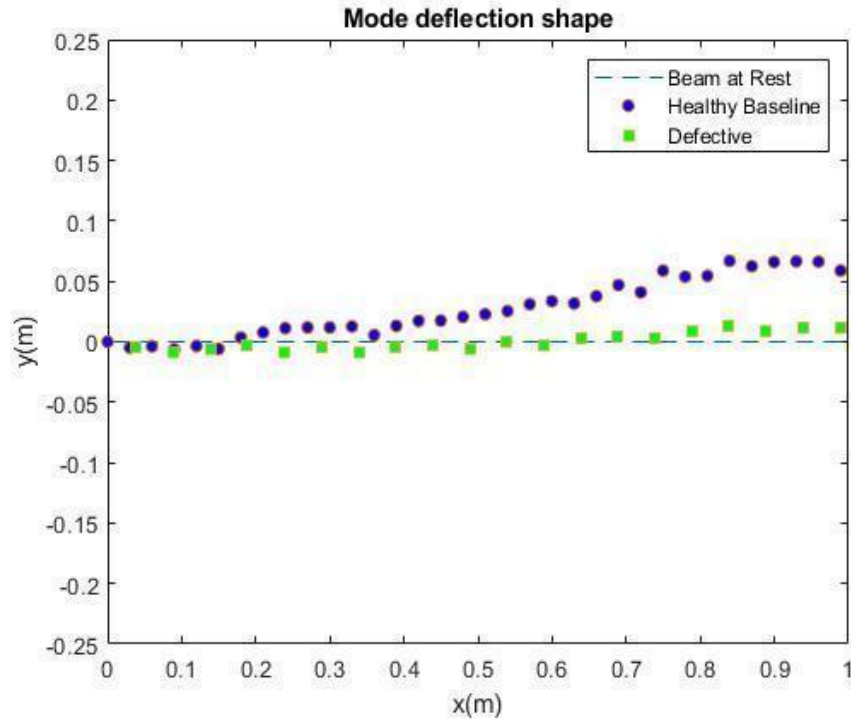


Figure 61: First Mode Shape of Defective GFRP Compared with Healthy Baseline at its Maximum Deflection

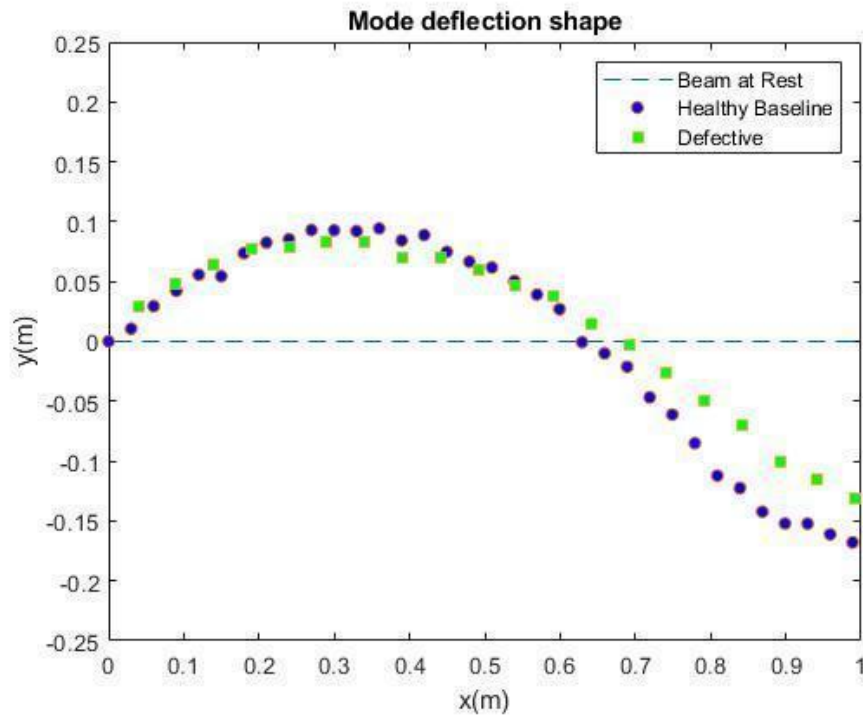


Figure 62: Second Mode Shape of Defective GFRP Compared with Healthy Baseline at its Maximum Deflection

To compare the operational mode shapes of the GFRP, the MAC value was used to quantitatively compare the baseline material with the defective material. The MAC value for the baseline provides a 98 % accuracy, while the defective yields approximately 55 % (Figure 63). This deviation of MAC value can be attributed to the change in the dynamic characteristics of the structure such as the effective mass or stiffness due to the presence of impurity in the material during manufacturing.

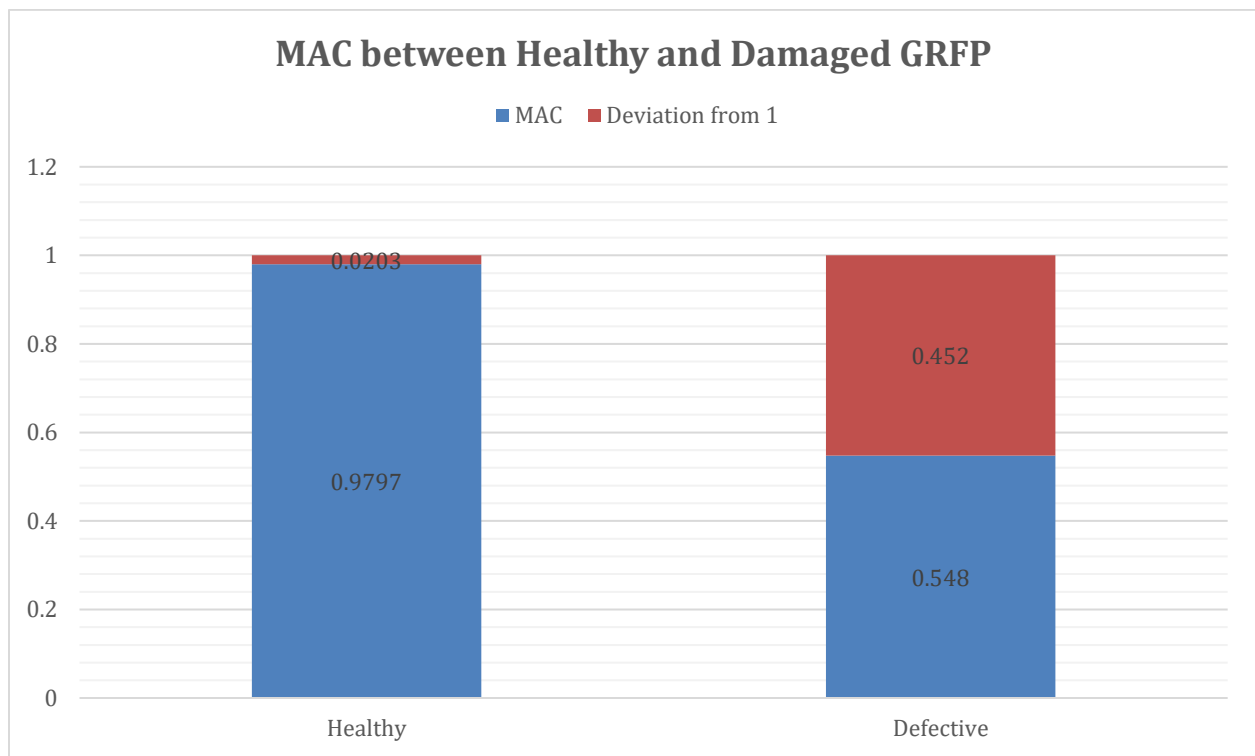


Figure 63: Estimated MAC Value of the Operational Mode Shapes of the Baseline and Damaged PLA

CHAPTER 6

CONCLUSION AND FUTURE WORKS

Conclusion

A damage detection technique was proposed utilizing video sources as an input to determine the damage characteristics. With the use of phase-based motion estimation and motion magnification algorithm the structural defects of PLA and GFRP structures were investigated. The results obtained by this approach were compared with the results from other conventional non-contact sensing methods used in SHM such as the LDS. The results yields a percentage accuracy of 99.6 %, indicating that the generated results from the two methods were in good quantitative agreement. The experimental results were compared with numerical simulation results using ANSYS.

Defects with different severity (0.1mm, 0.5mm, 0.7mm 1mm, and 1.5mm depth) and locations (60 mm, 90 mm and 120 mm from the fixed end of the structure) on a 3D printed PLA beam were measured using the phase-based approach. The structural analysis of composite structures such as Glass Fiber Reinforced Plastic was also carried out. By utilizing the phase-based motion estimation, the resonant frequencies and the dynamic characteristics of the structure were extracted. Changes in the resonant frequency were observed when the dynamic stiffness changed due to varying defects. The operational mode shape of the baseline and damaged structure was estimated using the motion magnification and edge detection algorithm. The experimentally obtained operational mode shapes are quantified by using the modal assurance criterion, which is shown to be a reliable damage index. The proposed method does not only produce an accurate result but also provides a better visual representation of the higher order structural modal characteristics.

Future Works

The phase-based motion estimation algorithm was observed to perform optimally when a small motion is involved. However, when large motions are involved, the resultant effects lead to an increase in the harmonics of the first order resonant frequency, making it challenging to extract other resonant frequencies. A more efficient algorithm that takes into consideration the effect of large motion could further improve the effectiveness of the proposed method.

The extraction of operational mode shapes from the magnified video involves a manual process of point selection due to inefficiency of the edge detection algorithm being used. More study needs to be done on improving the edge detection algorithm in a more sophisticated way to eliminate manual point selection.

Internal damage analysis was not performed during the course of this study. Future study to evaluate the effect of internal damage and non-uniform damages is suggested.

REFERENCES

- Abbood, Imad Shakir, Sief Aldeen Odaa, Kamalaldin F Hasan, and Mohammed A Jasim. 2021. "Properties Evaluation of Fiber Reinforced Polymers and their Constituent Materials used in Structures." *Materials Today: Proceedings*, vol. 43 (July): 1003 - 1008.
<https://doi.org/10.1016/j.matpr.2020.07.636>
- Bachmann, Jens , Yi Xiaosu, Gong Hugh, Martinez Xavier, Bugada Gabriel, Oller Sergio, Tserpes Konstantinos, Ramon Eric, Paris Christophe, and Moreira Pedro. 2018. "Outlook on ecologically improved composites for aviation interior and secondary structures." *CEAS Aeronautical Journal*, no. 9 (April): 533-543. <https://doi.org/10.1007/s13272-018-0298-z>.
- Belendez, T, M Perez-Polo, C Neipp, and A Belendez. 2005. "Numerical and Experimental Analysis of Large Deflections of Cantilever Beams Under a Combined Load." *IOP Publishing Ltd* (January). <https://doi.org/10.1238/Physica.Topical.118a00061>
- Belingardi, Giovanni , Ermias Gebrekidan Koricho, and Alem Tekalign Beyene. 2013. "Characterization and damage analysis of notched cross-ply and angle-ply fabric GFRP composite material." *Composite Structures*, vol. 102 (August) : 237-249.
<https://doi.org/10.1016/j.compstruct.2013.03.006>.
- Chen, Justin G, Oral Buyukozturk, and Heidi M Nepf. 2016. "Video Camera-based Vibration Measurement of Infrastructure." PhD diss., Massachusetts Institute of Technology, Cambridge.
- Chong, Yang, Fu Yu, Yuan Jian-ming, M. Guo, K. Yan, H. Liu, H. Maio, and Zhu Changchun . 2015. "Damage Identification by Using a Self-Synchronizing Multipoint Laser Doppler Vibrometer." *Shock and Vibration*, vol. 2015 (January) : 1 - 9.
<https://doi.org/10.1155/2015/476054>
- Coherent Market Insight. 2020. "Structural Health Monitoring Market Analysis." *Coherent Market Insight*. February 2020. <https://www.coherentmarketinsights.com/market-insight/structural-health-monitoring-market-3529> (accessed May 5, 2021).
- Dantec Dynamics. n.d. "Solid Mechanics DIC." <https://www.dantecdynamics.com/solutions-applications/solutions/stress-strain-espi-dic/digital-image-correlation-dic/> (accessed March 17, 2020).

Koricho, Ermias Gebrekidan, and Giovanni Belingardi. 2015. "An experimental and finite element study of the transverse bending behaviour of CFRP composite T-joints in vehicle structures." *Composites Part B: Engineering*, vol. 79 (September): 430-443.

<https://doi.org/10.1016/j.compositesb.2015.05.002>

Koslow, Tyler. 2016. "Carnegie Mellon University Research May Lead to Enhanced Design to Reduce Porosity in 3D Printed Titanium, Leading to Stronger Parts. ”.

<https://3dprint.com/135912/cmu-titanium-flaws/> (accessed May 7, 2020).

Molitch-Hou, Michael. 2017. "7 Issues o Look Out for in Metal 3D Printing. ”.

<https://www.engineering.com/3DPrinting/3DPrintingArticles/ArticleID/15202/7-Issues-to-Look-Out-for-in-Metal-3D-Printing.aspx>. (accessed June 5, 2020).

Peng, Cong, Cong Zeng, and Yangang Wang. 2020. "Camera-Based Micro-Vibration Measurement fo LightWeight Structure Using an Improved Phase-Based Motion Extraction." *IEEE Sensors Journal*, vol. 20, no. 5 (March): 2590-2599.

<https://doi:10.1109/JSEN.2019.2951128>.

Prakash, Arul, Kumar Sakthi, Mahan Tobias, McComb Christopher, Menold Jessica, and Conrad Tucker. 2019. "Detection of System Compromise in Additive Manufacturing Using Video Motion Magnification." *ASME: Journal of Mechanical Design* vol.142, no. 3 (December): 1-25.

<https://doi.org/10.1115/1.4045547>.

Energiforsk. 2020 "Optical Methods for Vibration Measurments in Nuclear applications." accessed June 20, 2020. <https://energiforsk.se/en/news-archive/optical-methods-for-vibration-measurements-in-nuclear-applications>.

Sarrafi, Aral, Zhu Mao, Niezrecki Christopher and Peyman Poozesh. 2018. "Vibration-based damage detection in wind turbine blades using Phase-based Motion Estimation and motion magnification." *Journal of Sound and Vibration*, vol.421 (May): 300-318.

<https://doi.org/10.1016/j.jsv.2018.01.050>.

Sause, Markus, Nora Schorer, Sebastian Gade, and Sinan Kalafat. 2016 "Advances In In-Situ Monitoring of Fiber Reinforced Composites." *17th European Conference on Composite Materials*.

Serraffi, Aral, and Zhu Mao. 2019. *Structural Dynamics Identification via Computer Vision Approaches*. PhD diss. University of Massachusetts, Lowell: ProQuest Dissertation & Thesis Global.

Simon, Baker, and Iain Mathews. 2004. "Lucas-Kenade 20 Year On: A Unifying Framework." *International Journal of Computer Vision*, vol. 56, No. 3 (March): 221-255.

Slotwinski, John, Garboczi J. Edward, and Keith M. Hebenstreit. 2014. "Porosity Measurements and Analysis for Metal Additive Manufacturing Process Control." *Journal of Research of the National Institute of Standards and Technology*, vol. 119 (September): 494–528.
<https://10.6028/jres.119.019>

Sturn, Logan D, Mohammed I. Albakri, Pablo A. Tarazaga, and Christopher B. Williams. 2019. "In situ monitoring of material jetting additive manufacturing process via impedance based measurements." *Additive Manufacturing*, vol. 28, (August): 456-463.
<https://doi.org/10.1016/j.addma.2019.05.022>

Strauss, Alfred, Roman Wan-Wendner, Marco Marcon, Pablo Castillo, Konrad Bergmeister, and Joan Casas. 2018. "Value of Health Monitoring in Structural Performance Assessment using Digital Image Correlation Systems." *Institute of Structural Engineering international*.

Wadhwa, Neal, Justin G. Chen, and Jonathan B.. Sellon. 2017. "Motion Microscopy for Visualizing and Quantifying Small Motions." *William H. Press*, vol. 114, no. 44 (August): 11639-11644. <https://doi.org/10.1073/pnas.1703715114>